
Article:
Afanasenkau, D., Kalinina, D., Lyakhovetskii, V. et al. (8 more authors) (2020) Rapid prototyping of soft bioelectronic implants for use as neuromuscular interfaces. Nature Biomedical Engineering, 4 (10). pp. 1010-1022. ISSN 2157-846X

https://doi.org/10.1038/s41551-020-00615-7

Rapid prototyping of soft bioelectronic implants for use as neuromuscular interfaces

Dzmitry Afanasenkau[1&], Dana Kalinina[2&], Vsevolod Lyakhovetskii[3,5], Christoph Tondera[1], Oleg Gorsky[2,3,5], Seyyed Moosavi[1], Natalia Pavlova[2,3], Natalia Merkulyeva[2,3,5], Allan V. Kalueff[6,7], Ivan R. Minev[1,8#*], Pavel Musienko[2,3,4,5#*]

[1]Biotechnology Center (BIOTEC), Center for Molecular and Cellular Bioengineering (CMCB), Technische Universität Dresden, Tatzberg 47-49, 01307 Dresden, Germany.
[2]Institute of Translational Biomedicine, Saint-Petersburg State University, Saint-Petersburg, Universitetskaya emb. 7/9, 199034, Russia
[3]Pavlov Institute of Physiology, Russian Academy of Sciences, Saint-Petersburg, emb. Makarova 6,199034, Russia
[4]Children's Surgery and Orthopedic Clinic, Saint-Petersburg State Research Institute of Phthisiopulmonology, Ministry of Healthcare of the RF, Saint-Petersburg, Politekhnicheskaya, 32, 191036, Russia
[5]Russian Research Center of Radiology and Surgical Technologies, Ministry of Healthcare of the RF, poselok Pesochnyy, Saint-Petersburg, Leningradskaya st., 70, 197758, Russia
[6]School of Pharmaceutical Sciences, Southwest University, Chongqing, China
[7]Ural Federal University, Ekaterinburg, Russia.
[8]Department of Automatic Control and Systems Engineering, University of Sheffield, Mappin Street, Sheffield, S1 3JD, United Kingdom.

[&]These authors contributed equally
[#]These authors contributed equally
* Corresponding authors; pol-spb@mail.ru (P.M.); i.minev@sheffield.ac.uk (I.R.M.).

Abstract
Neuromuscular interfaces are required to translate bioelectronic technologies for application in clinical medicine. Here, by leveraging the robotically controlled ink-jet deposition of low-viscosity conductive inks, extrusion of insulating silicone pastes, and in situ activation of electrode surfaces via cold-air plasma, we show that soft biocompatible materials can be rapidly printed for the on-demand prototyping of customized electrode arrays well-adjusted to specific anatomical environments, functions and experimental models. We also show that the printed bioelectronic interfaces allow for long-term integration and functional stability, for the monitoring and activation of neuronal pathways in the brain, spinal cord and neuromuscular system of cats, rats and zebrafish. The technology might enable personalized bioelectronics for neuroprosthetic applications.

One-sentence editorial summary:
Customized soft electrode arrays well-adjusted to specific anatomical environments, functions and experimental models can be rapidly prototyped via the robotically controlled deposition of conductive inks and insulating inks.

Introduction

Neural interfaces establish communication between biological systems and electronic devices. This technology can enable clinical applications for restoring physiological functions lost in injury or disease (*1-3*). A key aspect of biointegration of neural implants is their mechanical and anatomical adaptation to the neuronal environment. Recently, matching the elasticity of the implant to surrounding tissues of the nervous system has been recognized as crucial for long-term stability and biointegration (*4, 5*). This can be facilitated by the incorporation of elastic materials, mechanically adaptive thin films, foils and fibers into the implant, to allow close communication with the target tissues (*6-10*).
Despite improvements in materials, current technologies do not support rapid customization of implants. This makes adapting implants (to the varied anatomy of neural niches and the anthropometry of patients with different age, size, and specific therapeutic targets) impractical, costly and slow. Personalized medicine requires fast (on-demand) production of well-adjusted devices that enable physicians to design the optimal treatment strategy. Printing of medical devices has already been explored for various clinical applications, such as patient-specific artificial limb sockets, bone regeneration scaffolds and models for surgical planning (*11-13*). Although additive manufacturing has been applied for development of flexible and elastic bioelectronic devices for *in vitro* applications and external skins, rapid prototyping technologies for neural implants have not been applied (*14-17*). Here, we utilize the capacity of hybrid printing for integration of soft materials and composites into bioelectronic devices well-adapted to various anatomical structures and experimental models, in order to investigate, enable and recover functions of the neuromuscular system.

Results

We present a new technological algorithm to fabricate bioelectrode arrays from soft composite materials. For this, we applied robot-controlled deposition of conductive and insulating inks. To handle materials with diverse physical properties, we utilize extrusion, ink-jet and plasma surface activation in a single printing robot (**Fig. 1a, Supplementary Video 1**). The capacity for rapid prototyping, where the implant's layout as well as the number and the configuration of electrodes can be conveniently iterated, enables the customization of electrode arrays for specific applications in the neuromuscular system (**Fig. 1b**).

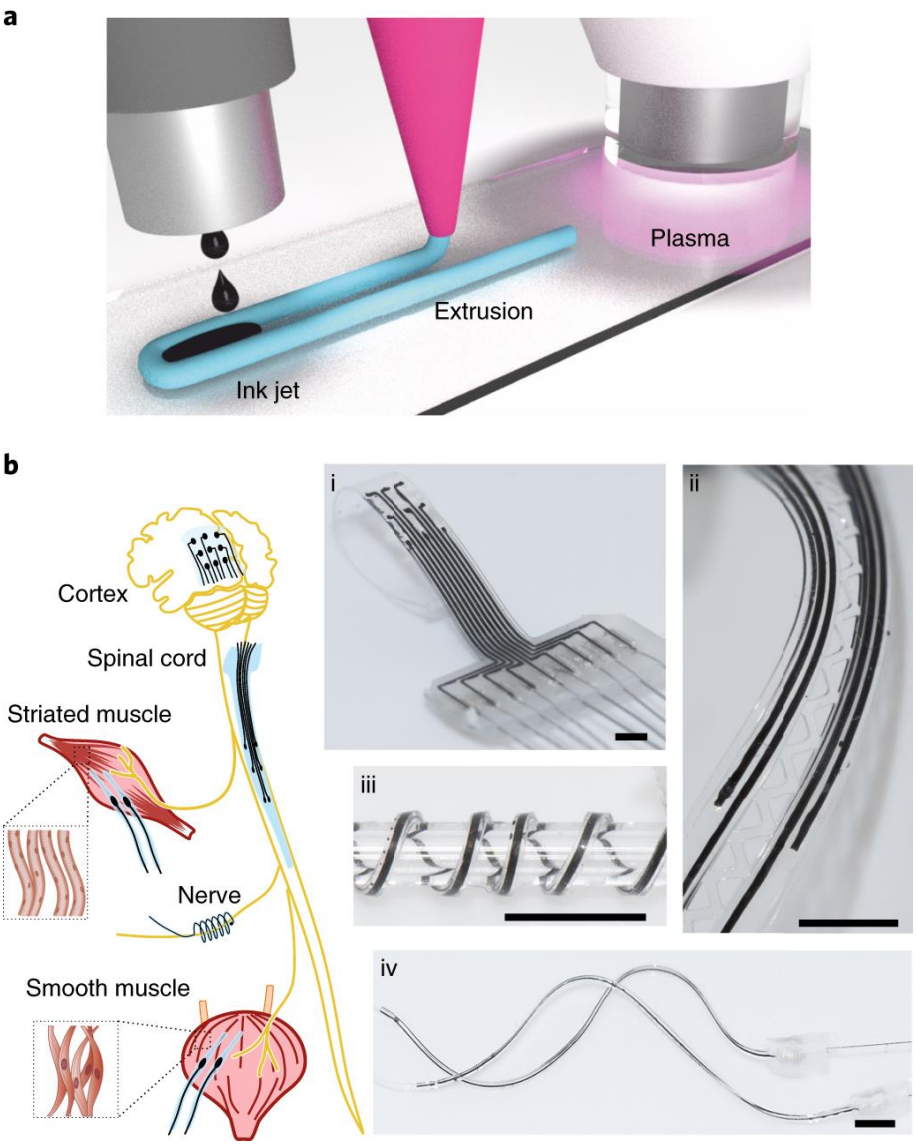

Fig. 1 | Rapid prototyping of soft electrode implants for interfacing the neuromuscular system. **a**, Integrated platform for hybrid printing combines ink-jet dispensing of low viscosity conductive inks, extrusion of insulating silicone pastes and in situ surface activation via cold air plasma. **b**, Electrode implants printed from platinum microparticles and silicone can be adapted to the anatomy of electrogenic tissues. Insets: *i* – cortical surface electrode array with 9 contact sites, *ii* – spinal surface electrode array with 4 contact sites, *iii* – peripheral nerve monopolar electrode, and *iv* – intramuscular shank electrodes with 1 contact per shank. Scale bars 4 mm.

The NeuroPrint technology: main steps, description and capabilities

Electrode arrays transmit signals to and from electrogenic tissues via distributed contact sites and interconnects that are embedded in an insulating matrix. Here, we apply multi-material printing to produce electrode arrays using elastic and biocompatible materials **(Supplementary Fig. 1, Supplementary Video 1)**. The insulating matrix is first structured by extrusion of a shear thinning silicone elastomer (SE1700, Dow Corning). This determines the overall geometry of the electrode array as well as the positions of tissue contact sites (**Fig. 2a *i-ii***) and the paths of interconnects (**Fig. 2a *iii***). Following the polymerization and plasma surface activation, the matrix becomes ready for deposition of electrical conduits via ink-jet. We next developed a custom ink where platinum microparticles (0.2-1.8 μm in diameter) are suspended in the viscous solvent tri(ethylene glycol) monomethyl ether (TGME, **Supplementary Fig. 2**), whose subsequent evaporation generates compacted platinum "sand" in the shape of the desired electrical conductor (**Fig. 2a, *iv***). Interfaces to external electronics are then formed by attaching flexible metal wires to contact pads by extrusion spotting of an electrically conductive paste (**Fig. 2a *v***). At the final step, a low-viscosity silicone Polydimethylsiloxane (PDMS, Sylgard 184, Dow Corning) is dispensed to form a conformal seal to the structure (**Fig. 2a *vi***). Due to its low surface tension, PDMS infiltrates spaces between particles in the platinum "sand" forming a composite material *in situ*. This is distinct from other methods where the conductive and elastomer phase are first mixed into a paste and then printed (*18*). The advantage of our approach is that the conductive particles in the "sand" are already forming a percolating network before PDMS infusion **(Supplementary Fig. 3)**. The Platinum

fraction in the composite is determined to be 80% by weight. Polymerization of the silicone phase results in a composite material with resistivity of $(9.8 \pm 1.5) \cdot 10^{-5}$ Ωm (n=4) which tolerates repeated cycles of tensile strain (**Supplementary Fig. 4**). Although nanoparticle based inks with lower resistivity have been reported in the literature, these typically contain silver and are deposited on non-elastic substrates (*19*). In integrated NeuroPrint arrays, electrical contact to tissue is facilitated at sites where platinum particles reach the surface (**Fig. 2b**). Our *in situ* composite formation process enables electrode arrays to be printed in arbitrary planar layouts at meso-scale integration density **(Supplementary Fig. 5)**.

Many applications require implants to mimic the viscoelastic properties of host tissues. In the NeuroPrint technology, this is enabled by the use of silicones and composites that ensure the overall stress-strain behavior of arrays remains comparable to that of soft tissues such as dura mater, peripheral nerve or muscle **(Fig. 2c)** (*20-22*). The range of deformations encountered *in vivo* vary by species and anatomical niche, however estimates of tensile strains in the nervous system rarely exceed 20%, beyond which tissue damage may occur (*23, 24*). In the physiological range of elastic deformation, NeuroPrint arrays exhibit stable stress-strain behaviour **(Fig. 2d)**. Similar to tissues, arrays may sustain changes when subjected to large tensile strains. In NeuroPrint arrays this may be attributed to Mullins softening typical of filled rubber composites and characterized by softening that depends on the peak strain encountered by the material (*25*). The ultimate tensile strain before mechanical failure exceeds 100% **(Supplementary Fig. 6)**.

NeuroPrint arrays maintain electrical functionality when subjected to physiologically relevant strains **(Fig. 3a)**, and following extended strain cycling (**Fig. 3b**). Strain induced electrical changes were not significant for the applications considered here and did not lead to implant failure. At the upper strain estimate of 20%, a nearly 10 fold increase in impedance is observed which translates to an absolute value of 20 kΩ (at 1kHz). This is at least two orders of magnitude lower than the input impedance of amplifiers typically used for neural recordings and is not expected to result in signal losses or distortion (*26*). Bending radii as small as 0.5 mm result in modest impedance increase <25% which facilitates wrapping of the electrodes around the geometry of small peripheral nerves **(Supplementary Fig. 7)**.

Electrochemically, NeuroPrint electrodes exhibit reduction and oxidation peaks typical of bulk platinum metal (**Fig. 3c**). The initial charge injection limit of contact sites is in the range of 150 to 250 $\mu C/cm^2$ (n=8 electrodes from two arrays) which is consistent with platinum neural electrodes of similar size (*27*). A moderate increase in the charge injection limit is observed following the application of 5M stimulation pulses which may be attributed to electrode surface activation **(Supplementary Figs. 8 and 9)** (*28*). Over 1 000 stretch cycles we observe a general trend of decrease in the charge injection limit but as with impedance measurements no catastrophic failure of any of the electrodes was seen **(Fig. 3d).** The electrochemical stability and resilience to mechanical deformation makes NeuroPrint electrodes suitable for applications requiring stimulation of electrogenic soft tissues.

Our hybrid printing approach generates minimal waste because the conductive sand is deposited with high precision only where conductivity is required. This facilitates the use of relatively more expensive metals such as Platinum for applications where biocompatibility requirements restrict the range of available materials. However, the fabrication process can be generalized to lower cost conductive materials. To demonstrate this, we used Silver nanowires (AgNW) to print electrodes of similar dimensions which retain key electrical functionalities needed for bioelectronic interfacing applications **(Supplementary Fig. S10)**. Our printing method is amenable to the introduction of emerging materials such as hydrogels or conductive polymers that hold promise for decreasing electrode impedances and improving implant biointegration (*29, 30*).

With their simple construction, NeuroPrint electrodes eliminate the need for cleanroom processing and the development of design-specific masks and fabrication tools which are typically employed for the production of neural probes (*31*). Typical production time from design specification to a finished prototype can be as short as 24 h, thereby enabling the production of custom implants on demand.

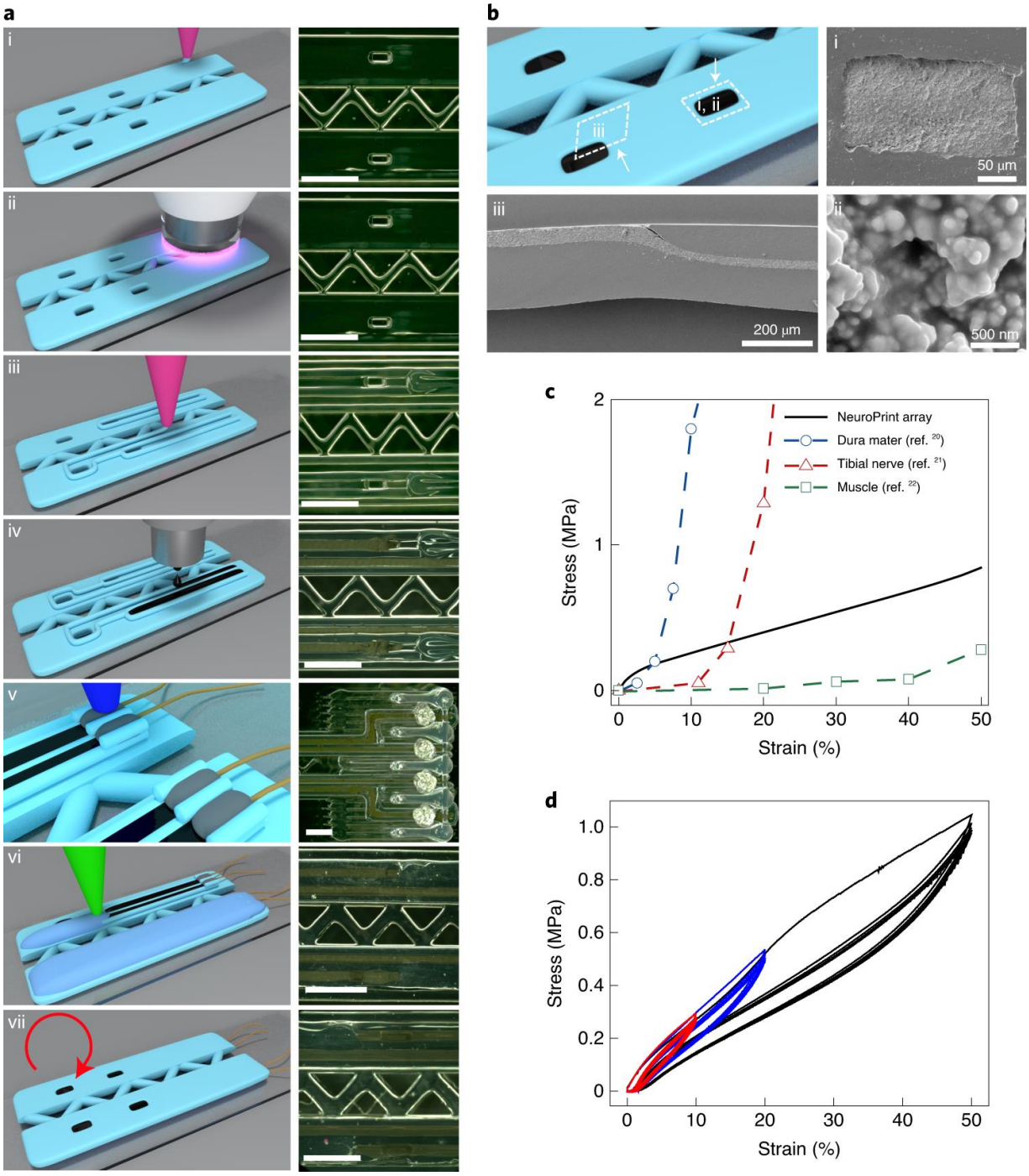

Fig. 2 | Printing and mechanical properties of planar electrode arrays.
a, Schematic representations (left) and optical micrographs (right) of each step in the hybrid printing process. Positions of the electrode active sites are defined (*i*). The "zig-zag" line in the middle defines a mesh – a design feature included to aid diffusion of interstitial fluids through the implant. Plasma activation is applied to enhance the wettability of the surface (*ii*). Borders to limit the spread of the platinum suspension are printed (*iii*). A liquid suspension of Platinum microparticles is deposited via ink-jet (*iv*). To assemble a connector, wire guides (silicone SE1700) and a conductive paste (Epo-Tek H27D, part A) are printed by extrusion. Electronic wires are inserted in the guides by hand (*v*). A final seal of low viscosity PDMS (Sylgard 184) is applied (*vi*). Following thermal polymerization, the finished electrode array is peeled from the printing substrate and inverted (*vii*). The scale bar in the micrographs is 1 mm. **b**, Scanning electron micrographs: of a contact site as seen from above at low (*i*) and high (*ii*) magnification. A cross section through the thickness of an array illustrates an embedded interconnect and contact site (*iii*). **c**, stress strain behavior of explants of various soft tissues is compared to a typical NeuroPrint array. Data for biological tissues is extracted from Noort et al, 1981 [20], Kwan et al, 1992 [21] and Calvo et al, 2010 [22]. **d**, stress-strain responses of a typical NeuroPrint array subjected to a cyclic uniaxial strain ramp. Five consecutive strain cycles are performed for each of the peak strains (10%, 20% and 50%). For **c** and **d**, the gauge length of the arrays is 10 mm and the rate of elongation is 0.1 mm/s.

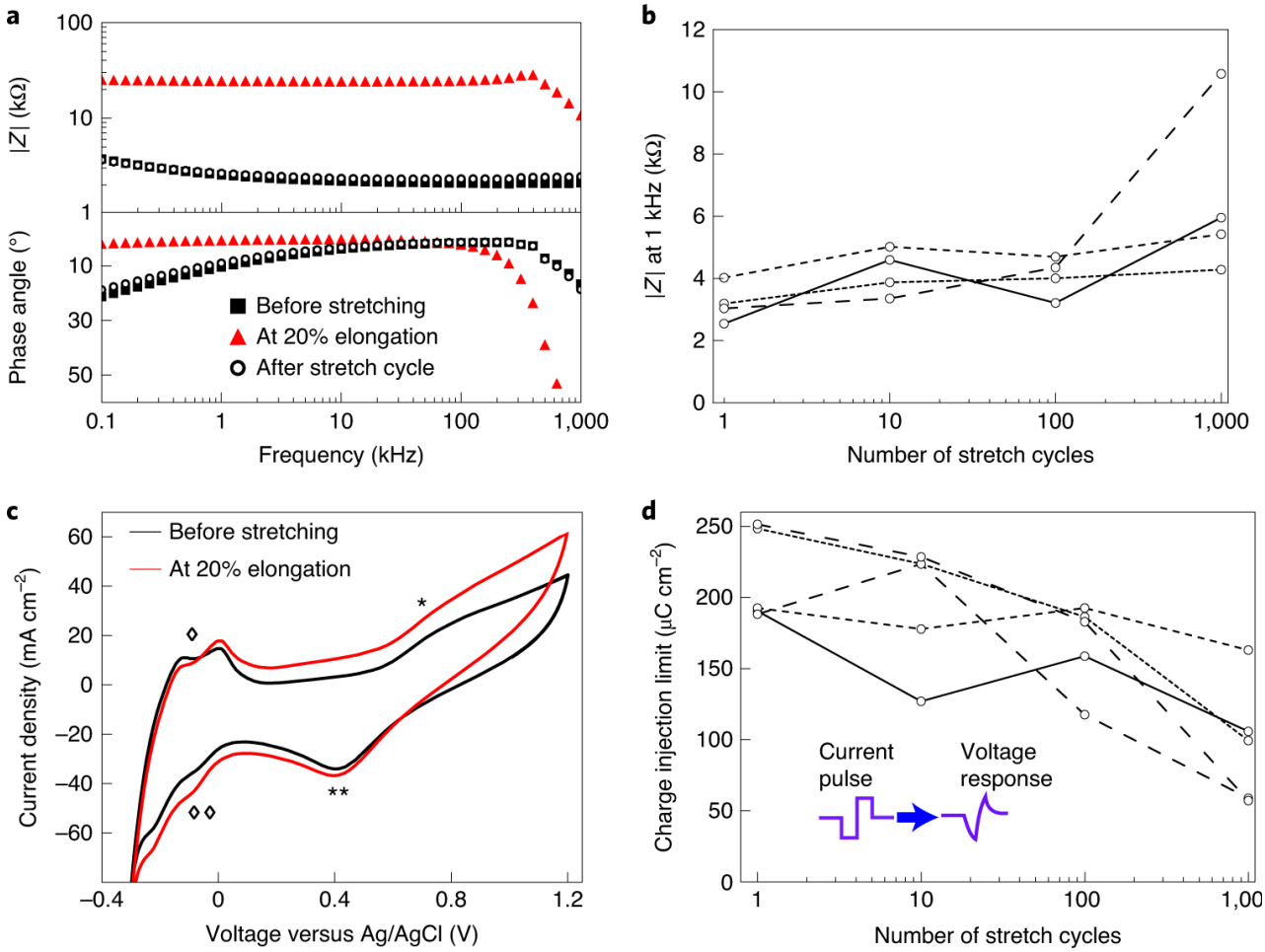

Fig. 3 | Electromechanical properties.
a, Modulus and phase angle of electrode impedance recorded in phosphate-buffered saline. Spectra were recorded before stretch (■), at 20% uniaxial tensile strain (▲), and following relaxation to 0% strain (○). The area of the electrode is 2.6×10^{-4} cm^2. **b**, Impedance modulus of electrodes subjected to uniaxial fatigue cycling. Impedance is recorded at 0% strain following the completion of the previous strain cycle. The maximum strain encountered during each fatigue cycle is 20%. Each line represents a single electrode. **c**, Cyclic voltammograms recorded in diluted sulfuric acid (300mM), at 1V/s vs Ag/AgCl. Peaks correspond to oxide formation (*), oxide reduction (**), H^+ adsorption (◇◇), and H^+ desorption (◇) on Pt microparticle surfaces. **d**, charge injection limits of electrodes subjected to uniaxial fatigue cycling. The charge injection limit is recorded at 0% strain following the completion of the previous strain cycle. The maximum strain encountered during each cycle is 20%. Each line represents a single electrode.

NeuroPrint implants enable multi-nodal activation and monitoring of the neuromuscular system

To validate functional capacities of NeuroPrint technology, we produced a library of designs (**Fig. 1b, Supplementary Fig. 11**) covering a range of applications, including the activation of the spinal locomotor system in motor impaired animals (*32*), recording striated and smooth muscles, and interfacing sensorimotor and visceral networks (**Fig. 4a**). All electrode array designs produced have thickness of approximately 200 µm. The softness and well-adjusted geometry of the implants allowed us to optimize the surgical procedures in order to access peripheral nerves, detrusor and limb muscles, subdural space of the spinal cord and sensorimotor cortex in different animal models.

Electrical spinal cord stimulation (SCS) is a highly efficient method for experimental and clinical neurorehabilitation (*33, 34*). It is essential, however, to identify the underlying mechanisms of the therapeutic effects and further optimize the implanted devices and stimulation algorithms. Here, we show that NeuroPrint electrode arrays are efficient for this task *in vivo* (**Fig. 1b, Fig. 4**). Specifically, continuous SCS (5Hz, 0.2ms) of sacral cord (S1-S3) evoked locomotion of decerebrated cats (n=4 cats) with reciprocal activation of flexor and extensor muscles, good foot placement and well-coordinated hind limb movements in step cycle (**Fig. 4b,c, Supplementary Video 2**). Compared to a conventional wire, NeuroPrint intra-muscular electrodes demonstrate a similar quality of the electromyographical (EMG) signals during stepping activity (**Fig. 4c**). Furthermore, SCS of different rostro-caudal and medio-lateral locations triggered local neuronal networks responsible for specific left-right and rostral-caudal EMG pattern activation (**Fig. 4d,f, Supplementary Video 2**) that is essential for spatiotemporal neuromodulation treatment after SCI (*35*).

We next wrapped stimulating NeuroPrint electrodes around a section of the cat sciatic nerve (running in the proximal part of the hip), and performed simultaneous recording of ElectroSpinoGram (ESG) and EMG activity (n=4 cats). Activation of fast-conducting sensory and motor fibers in the sciatic nerve evoked waveforms with varied latency **(Fig. 5a,d)** in the spinal cord and gastrocnemius muscle, whose shape and amplitude depended on the intensity of stimulation**.** We also found that the ESG-evoked potentials were modulated by the side of sciatic nerve stimulation, as well as by the distance between the recording and the stimulation sites **(Fig. 5b,c).** We also observed the classical reflex dynamics of the H-wave suppression by the M-wave (*36*), as the amplitude of sciatic nerve stimulation increased **(Fig. 5e)**. Thus, multi-nodal monitoring of evoked potentials with distributed NeuroPrint electrodes enabled neuromuscular activation on the systems level (*36*). We next applied NeuroPrint electrode arrays to record ESG for extracting the activation pattern of distributed neuronal pathways **(Supplementary Fig. 12)** during cat stepping (n=4) in response to stimulation of the mesencephalic locomotor region (*32, 37*). Finally, we confirmed that the NeuroPrint technology can be applied to other physiological systems and animal models. For example, implanting a pair of EMG electrodes in the smooth detrusor muscle of the cat urinary bladder (n=4), we recorded its activation in the voiding stage of the urodynamic cycle during intravesical saline infusion **(Fig. 5f)** (*38*). In a different model organism, the zebrafish *Danio rerio* (n=5), we access the swimming network by inserting adapted NeuroPrint electrodes in the dorsal muscles and recorded the EMG bouts when the fish swam actively **(Fig. 5g)** (*39*).

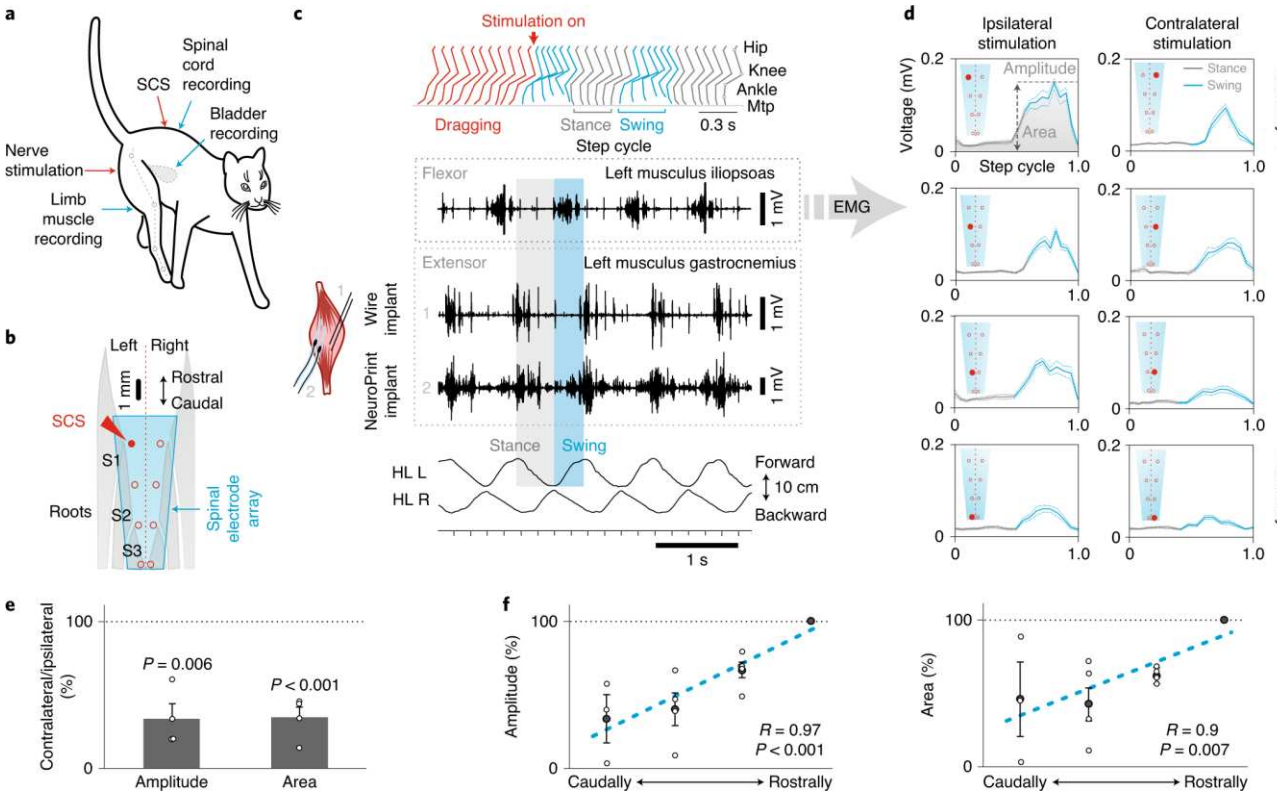

Fig. 4 | Neuromodulation of the locomotor circuitry using NeuroPrint technology.
a, Range of applications demonstrated in the decerebrated cat model include spinal cord stimulation, recording of striated limb muscle and smooth detrusor muscle, ESG recording and peripheral nerve stimulation. **b**, Locations of spinal cord and root stimulation (S1-S3, 5Hz, 0.2ms). **c**, Cycle of locomotion evoked in a decerebrated cat. Reciprocal activation of flexor and extensor muscles and coordinated hind limb movements can be observed. HL L and HL R indicate left and right hind-limbs. **d-f**, Electrical stimulation at various rostro-caudal and medio-lateral locations evoked different patterns of hindlimb muscles activation during a step cycle. Average (n=4 cats, 1 SE, shaded area) rectified signals from left hip flexor iliopsoas muscle activity during the stance and swing phases of gait **(d)**, and the average amplitudes and area (square under the curve) in relation to the ipsilateral stimulation **(e)** show that left electrodes (ipsilateral to the muscle) evoked higher locomotor bursts during the swing phase, and more rostral stimulation locations (over the S1-S3 spinal cord segments and roots) increased the activity of the muscle **(f)**. Significance in e-f was determined using paired two-tailed t-test.

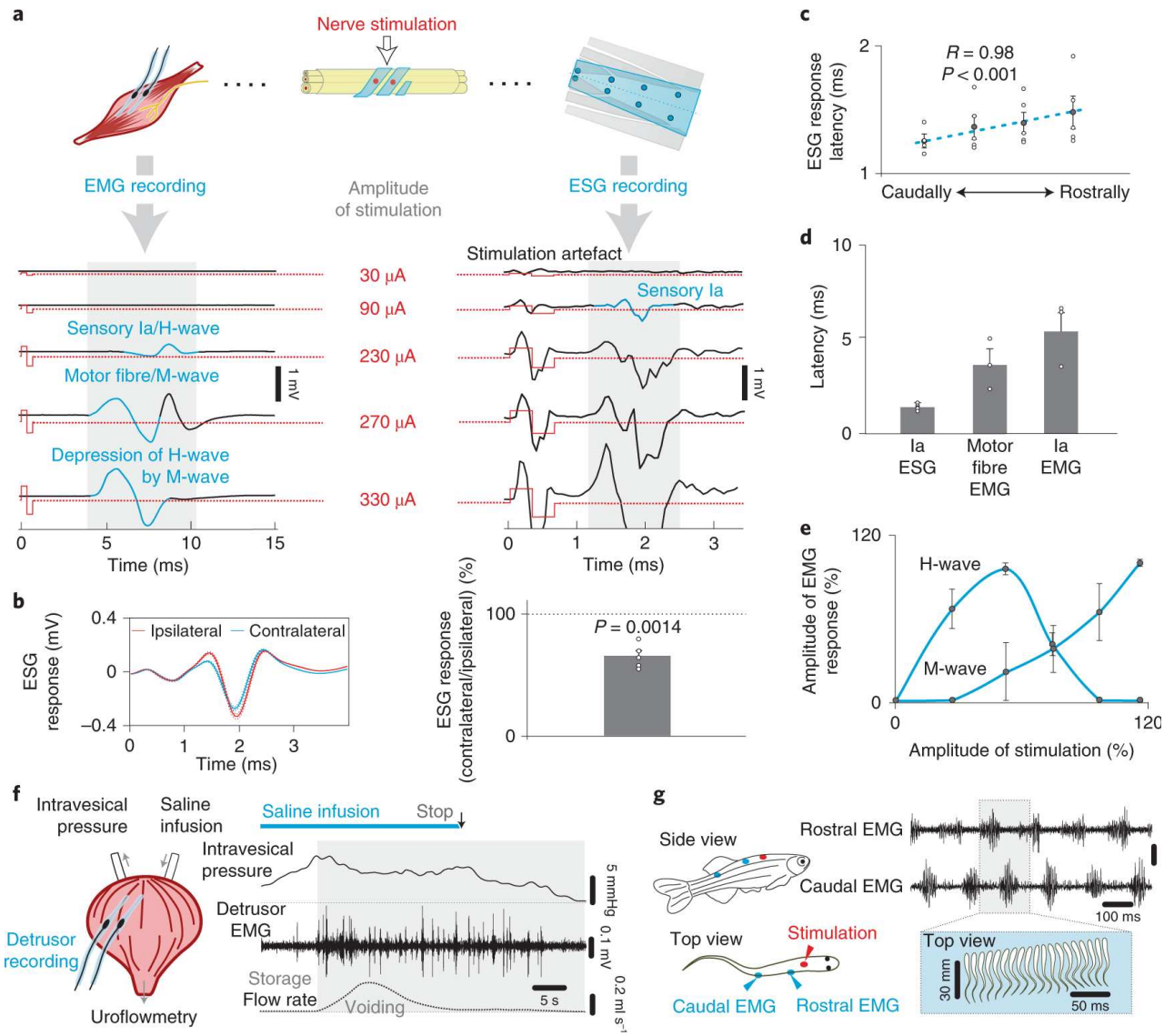

Fig. 5 | Multi-nodal activation and monitoring of the neuromuscular system using NeuroPrint technology. **a-e**, Mixed sciatic nerve stimulation (1Hz, 0.2ms), ESG recording and EMG recording in medial gastrocnemius muscle allowed multi-nodal access to sensorimotor system (n=5 cats). **a**, Waveforms generated by the sequential recruitment of fast-conducting proprioceptive, sensory and motor fibers in the sciatic nerve. **b**, The amplitude of contralateral short-latency ESG evoked potentials in relation to ipsilateral evoked by sciatic nerve stimulation. **c**, The latency of ESG signals is observed to depend on the rostro-caudal position of the recording electrode. **d,** Latencies observed at various recording nodes indicate direct- (Ia ESG and motor fibers EMG) and mono-synaptic (Ia EMG) responses to sciatic nerve stimulation. **e**, Sciatic nerve activation reveals the classical H-wave suppression by the M-wave. **f**, Detrusor activity recorded by NeuroPrint electrodes during urodynamic testing. Increased activity of the detrusor muscle can be observed following saline infusion to the cat bladder. **g**, Spinal cord stimulation and EMG recording of two dorsal muscles (rostral and caudal) demonstrates the capability of the soft electrodes to access the swimming network in a zebra fish model. Significance in b-c was determined using paired two-tailed t-test.

Long-term biointegration and functional stability of the NeuroPrint technology

We then tested long-term biocompatibility and functional stability of NeuroPrint interfaces in a rat model, utilizing this approach in one of the most delicate anatomical locations of the nervous system (**Fig.6a**). Specifically, spinal electrode arrays (**Figs. 1b** and **6a**) were implanted in the intrathecal space where repeated mechanical loading commonly places high demand on their resilience. We considered that if subdurally implanted NeuroPrint electrodes (**Fig.6a**) do not affect the functional and morphological aspects of nervous system, then other implantation locations are likely to be safer. Our design included “mesh” pattern as a specific feature for improving its incorporation into the surrounding tissue **(Supplementary Fig. 11)**, with the stable position lasting for several weeks of testing. The behavioral capacities and histological slices from implanted (n=4) and sham (n=4) rat groups of animals were assessed 8 weeks after surgery (**Fig. 6b-i**). Sham-operated animals received the same surgical procedures (head-plug fixation, laminectomy and vertebral orthosis) without spinal implants.

Overall, there were no significant differences between the two groups in histological (**Fig. 6c-f**) and behavioral data (**Fig. 6g-i, Supplementary Video 3)**. As an indicator of neuroinflammation, we analyzed the expression of the microglial marker *Iba1* in spinal cord sections (**Fig. 6e**). For the histological analysis, the total number of microglial cells was evaluated both using manual counting (**Fig. 6e**) and relative area/optical density technique (**Fig. 6f, Suppl. materials**). The ratio of resting *vs* activated glial cells (**Suppl. Fig. 13, Suppl. materials**) was also assessed (*40, 41*). No significant differences between the two groups were obtained (**Fig. 6b-e, Suppl. Fig 13**). In addition to general abilities to move on the ladder (**Fig. 6g,h**) and run on the treadmill belt with low to high speeds (**Fig. 6i; Supplementary Video 3**), we monitored fine aspects of the sensorimotor activity including forelimb/hindlimb coordination (**Fig. 6i,j**; **Suppl. Fig. 14a,f**), timing of the step cycle (**Fig. 6p**), step width (**Suppl. Fig. 14 c,d)**, length (**Fig. 6q; Suppl. Fig. 14e),** height (**Fig. 6j,k**) and their variability (**Suppl. Fig. 14 g,h**). These parameters were not affected in subdurally implanted vs sham rats (**Suppl. Fig. 14b)**. Finally, we analyzed the postural capacities (**Fig. 6l-n; Suppl. Fig. 15**) of the rats during locomotion (*42*). This function is dependent on multiple sensory and motor networks in the brain and spinal cord which are very sensitive to impairment in neurological disorders, trauma and neurotoxic conditions (*43*). We assessed the mediolateral displacement of the body center of mass (**Fig. 6l,m, Suppl. Fig. 15a)**, lateral foot placement (**Fig. 6n)**, and performed correlation analysis between the lateral displacements and corresponding foot position **(Suppl. Fig. 15b)**. All these parameters reflect the efficacy of dynamic balance control during locomotion (*42, 44*) and were similar in sham and implanted groups. These results confirm the absence of gross and fine motor deficits or balance impairments resulting from the implant and indicate a good level of biointegration at 8 weeks.

The functionality of electrodes was evaluated weekly by testing their impedance (**Fig. 7a**) and current thresholds for muscle recruitment (**Fig. 7b,c**). Out of 16 electrodes implanted in 4 rats, 14 maintained finite impedances and the ability to induce evoked muscle potentials. In the first two weeks, we also observed a trend for increased impedances and current thresholds that may be attributed to the formation of connective tissue (**Fig. 7a,b**). We then tested the functional state of neuronal pathways located in close proximity to implants (**Fig. 6a; Fig. 7d-h; Suppl. materials**). At the chronic stage (8 weeks), the NeuroPrint spinal interfaces (n=4) were used for recording task-specific ESG in behaving rats (**Fig. 7d, Supplementary Fig. 16),** and the implants maintained site-specific neuromodulation capacities of the sensorimotor network (**Fig. 7e, Supplementary Fig. 17)**. Collectively, this indicates the high level of their biointegration and their stable location relative to targeted spinal pathways. Finally, using brain NeuroPrint array adapted for the rat sensorimotor cortex (**Fig. 7f; Suppl. Fig. 11)**, we extracted cortical states during locomotor activity **(Supplementary Fig. 18)** and probed pathways responsible for ascending and descending brain-spinal communication (**Fig. 7g,h**) (n=5).

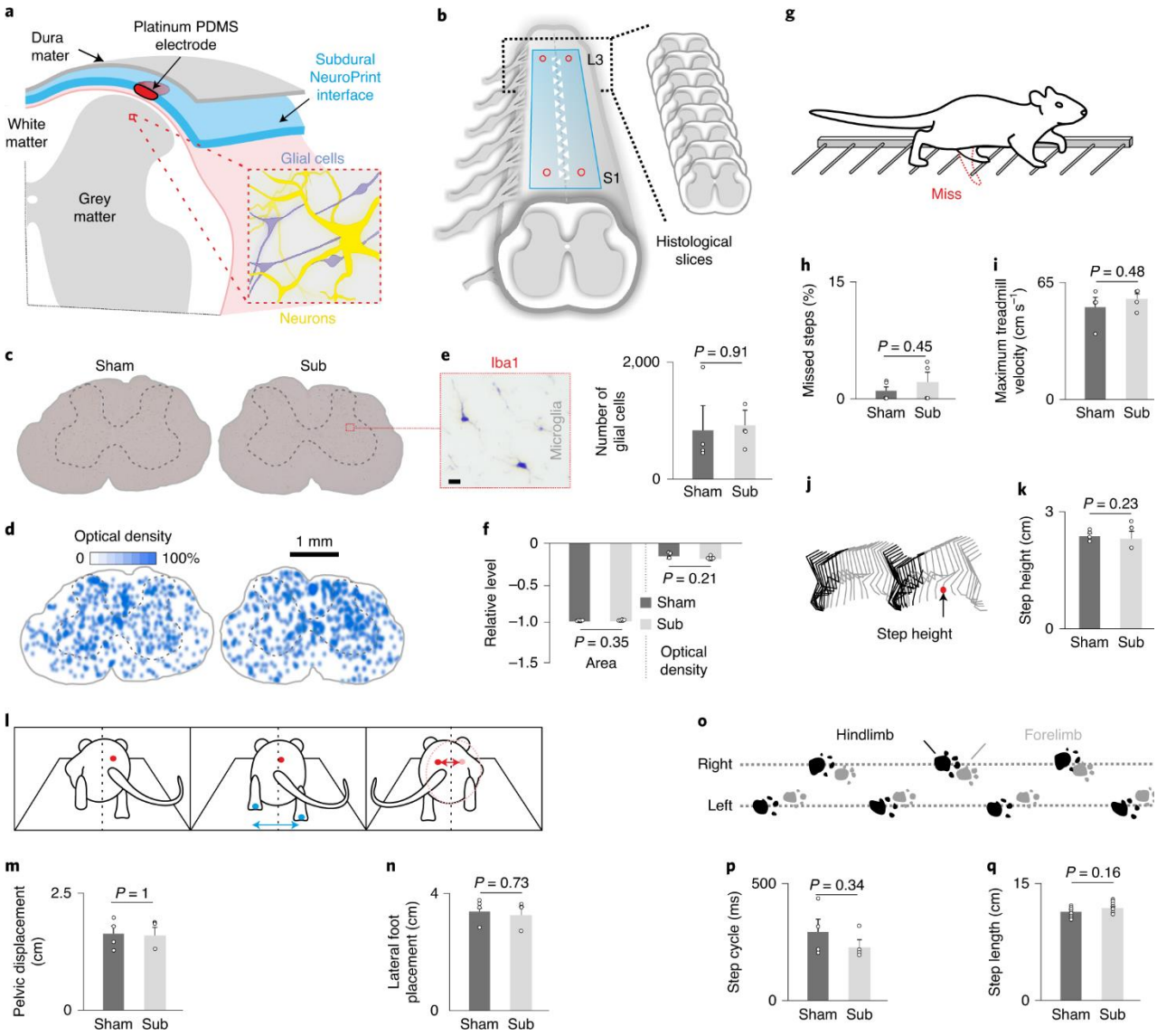

Fig.6 | Biointegration of NeuroPrint electrode arrays.
a, Schematic cross section of the spinal cord with the NeuroPrint implant inserted in subdural space, and the neuronal network as well as glial cells in close proximity to Pt-PDMS electrode. **b-f**, Immunohistochemical evaluation of neuroinflammation at 8 weeks post implantation. **b**, Spinal cord tissue located under the implants was sectioned into transverse slices. **c**, Contours of representative slices from sham operated and NeuroPrint implanted spinal cords. **d**, Normalized optical density of spinal cord slices labeled for microglia by Iba-1 antibody conjugated gold nanoparticles. **e**, A representative slice fragment containing stained microglia (left) and total amount of the manually counted glial cells per slice (right). **f**, Relative area (left) and optical density (right) of pixels belonging to the glial cells. **g-i**, Quantification of motor impairments 8 weeks after implantation. **g**, Ladder task for assessment of fine hind limb motor control. **h**, Mean percentage of missed steps averaged across all animals and trials (n = 8 trials per rat, n = 4 rats per group, ns). **i**, Maximum treadmill velocity that rats can walk (n = 8 trials per rat, n = 4 rats per group). Side-view **(j)** of the rat stepping on the treadmill belt, the red dot indicates metatarsus position which was used to analyze the step height **(k)**. **l-n**, Postural balance and coordination during locomotion 8 weeks after implantation in implanted and sham groups of animals (n = 20-40 step cycles per rat, n = 4 rats per group). Back view of the rat stepping on the treadmill belt **(l)**, red and blue dots indicate pelvic displacements **(m)** and lateral foot placements **(n)**. **o,** Footprint-test shows position of the hind limbs and fore limbs from the bottom to measure fine aspects of locomotor control on the runway. Duration of the step cycle **(p)** and step length **(q)** in implanted and sham groups of animals. Significance in h, i, k, m, n, p, q was determined using unpaired two-tailed t-test.

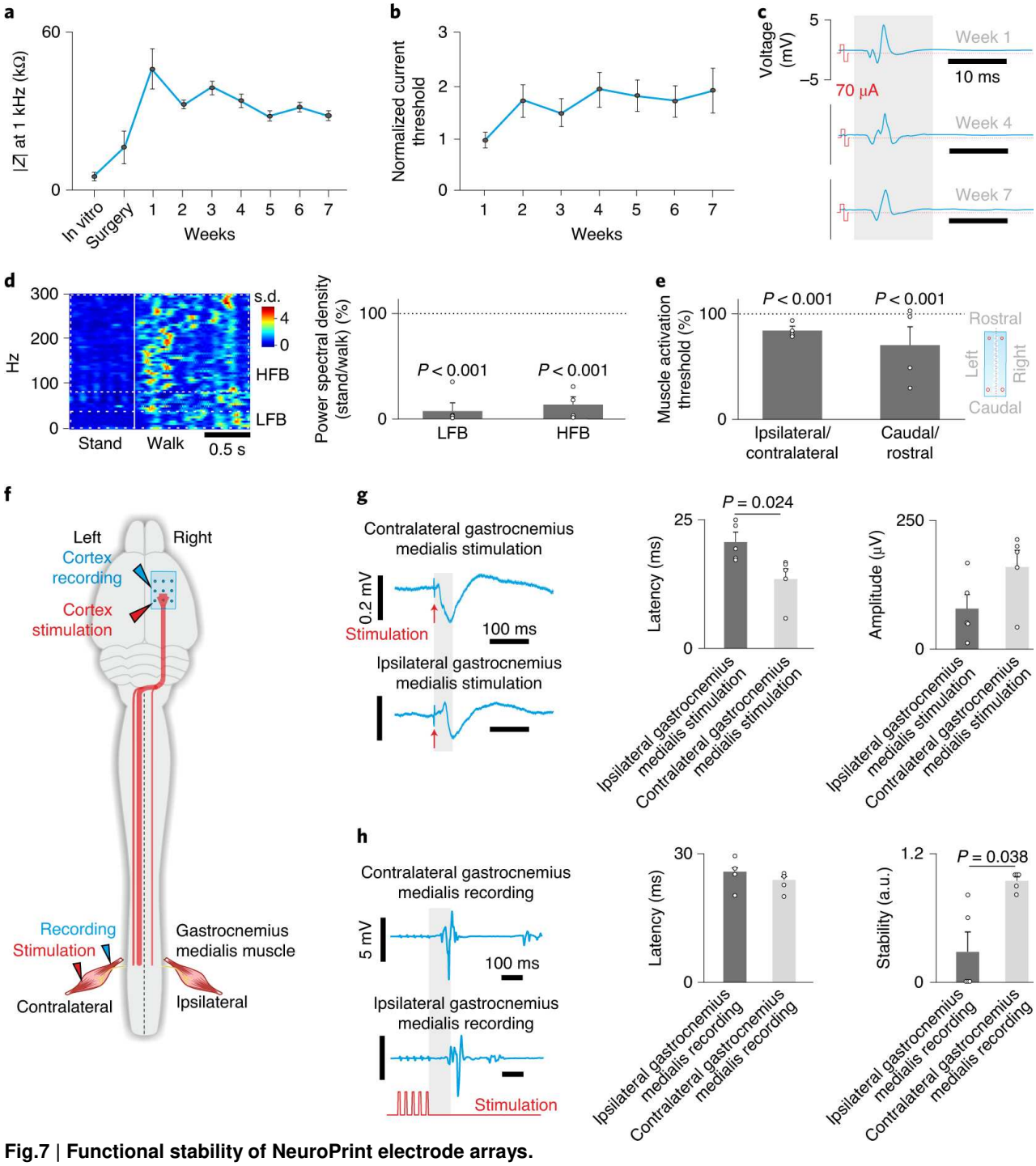

Fig.7 | Functional stability of NeuroPrint electrode arrays.
a-h, Evaluation of implant functional stability 6-8 weeks post implantation. **a**, Electrode impedance modulus measured at 1 kHz (n = 14 total electrodes across four rats) recorded in vitro, immediately after implantation and then weekly. Surg. – intraoperative testing, just after surgical implantation. **b**, Dynamics of normalized current thresholds of the evoked potentials in extensor muscle gastrocnemius medialis. **c**, Representative gastrocnemius medialis EMG waveforms evoked by spinal cord stimulation at weeks 1, 4 and 7. **d**, Task-specific spinal cord recording during standing and walking. **e**, Muscle activation thresholds during stimulation (1Hz, 0.3ms) of different sites of the spinal cord. Ratio of ipsilateral to contralateral and caudal (S1) to rostral (L3) stimulation of the muscle (n=4 rats). **f**, NeuroPrint implants are positioned over the sensorimotory cortex and in the gastrocnemius medialis muscles of the hind limbs. **g**, Electrocorticographic recordings of somato-sensory potentials evoked by ipsilateral (right) and contralateral (left) GM stimulation. The latency and amplitudes of signals are presented in the center and right panels respectively (n=5 rats). **h**, Electromyographic recordings in GM (ipsilateral and contralateral) of potentials evoked by motor cortex stimulation (left). Latency of signals recorded in the ipsilateral and contralateral GM (center). Proportion of stimulation pulses that evoke a response (stability) in GM muscles (right) (n=5 rats). Significance in d, e, g, h was determined using paired two-tailed t-test. Key: sham – control group, sub – subdural implantation. ns – non-significant.

Discussion

Overall, here we present a hybrid printing technology to produce interfaces for monitoring and enabling functional states of the nervous system. Due to adapted geometries and mechanical softness, the NeuroPrint interfaces can be applied to various neural structures, model species and tasks. Using a variety of electrode configurations, we stimulated and recorded biopotentials from the brain, spinal cord, peripheral nerve, as well as striated and smooth muscles.

The electrode designs are informed by anatomical measurements performed in the various models and neuromuscular subsystems we targeted. This level of adaptation is not available from state-of-the art electrode arrays. As an example, pre-clinical neuroprosthetic systems employing spinal cord stimulation are a promising treatment for paraplegia. However, they rely on implantable epidural electrodes developed for treating neuropathic pain (*1, 45*). This imposes a limitation on the specificity with which sensorimotor pools can be targeted because the electrode positions are rigid. In a future clinical scenario, optimal intervention may depend on adapting the stimulation pattern on the idiosyncrasy (e.g. spinal level, severity etc.) of the injury as well as fine anthropometric adjustments. Personalized implants may thus be linked to better clinical outcomes. As a meso-scale fabrication technology, NeuroPrint is well suited to the circuits-level interfacing. The technology may find applications for rapid prototyping of integrated networks of biological sensors and actuators (*46, 47*). The monolithic infrastructure combined with mechanical elasticity ensured resilience to mechanical deformation and efficient charge exchange with neural structures under chronic implantation. Conductive silicone composites are an emerging material for *in vivo* bioelectronics and need to be studied further. Tissue histology and functional studies performed by us and others suggest that such materials are structurally stable for long term implantation (*5, 48*). Electromechanical properties of the implants enabled their biointegration in long-term *in vivo* experiments, suggesting their potential applications in different fields of translational and clinical neuroscience, including neuroprosthetics and electroceuticals and brain machine interfaces (*49*).

Outlook

To test chronic biocompatibility we chose a subdural location for the implant where electrodes make close contact with targeted neuronal circuits (**Fig.5a**). An important advantage of such location is improved spatial specificity and access to the intrathecal space. In future designs these advantages can be used to deliver tailored pharmacological neuromodulation, neuroregeneration and anti-inflammation therapy. The present study confirms that even in delicate anatomical locations, NeuroPrint technology can establish communication with the neuromuscular system. We demonstrate low levels of neuroinflammation, absence of general neurotoxic effects and functional preservation of adjacent neuronal circuits. Although additional studies to develop specific devices and systems for clinical use and testing of their biocompatibility are needed we showed the potential of on-demand and flexible fabrication technologies for producing highly personalized devices for bioelectronic medicine.

Methods

Hybrid printing. Printing was performed using the 3D Discovery bioprinter from RegenHU (Villaz-St-Pierre, Switzerland). The device incorporates four printing heads, enabling different printing modes within one printing procedure **(Supplementary Fig. 1**). For printing silicones, we applied a printing head, which utilizes air pressure to extrude material through a nozzle. We used a conical nozzle with 110 µm inner tip diameter for printing the silicone elastomer SE1700 (Dow Corning), and a 6 mm cylindrical nozzle with 150 µm inner diameter, for extruding the silicone elastomer Sylgard 184 (Dow Corning). The conductive epoxy (Epo-Tek H27D, part A) used for making contacts was extruded through a 410 µm conical needle (All needles where obtained from Poly Dispensing Systems, Inc., Orgeval, France). The Platinum suspension ink was printed using a solenoid actuated ink-jet microvalve with nozzle diameter 0.1 µm (SMLD 300G, Fritz Gyger AG, Gwatt, Switzerland). For plasma activation of the surface, we installed a portable cold-plasma generator Piezobrush® PZ2-i equipped with a nearfield nozzle from Relyon Plasma (Regensburg, Germany) in place of one of the printing heads. Models for printing were designed using a custom-made Python-based software, which allowed us to modify and visualize G-code (used to control the printer) as well as incorporate variables into the code.

Ink preparation and loading. *Silicones.* Silicone elastomers, SE 1700 and Sylgard 184 (Dow Corning), were prepared by mixing catalyst and base at a ratio of 1:10 w:w and loading the mixtures in Luer lock equipped printing syringes. This is followed by centrifugation to remove air bubbles (Eppendorf Centrifuge 5910 R, S-4xUniversal Rotor, 3000rpm, ~1min).

*Platinum ink preparation for ink-jet printing***.** Platinum particle ink is prepared by mixing 400 mg of platinum powder (particle diameter 0.2-1.8 µm, Karlsruhe, Germany) with 4 ml of tri(ethylene glycol) monoethyl ether (TGME, Merck KGaA) in a 50 ml Falcon tube, followed by tip sonication (BRANSON Digital Sonifier W-450D with 1/8 ’’ Tapered Microtip, 10% of power, 10 s/10 s sonication/delay time, total time > 30min). Sonication

decreases the size of platinum particle aggregates, thereby making the suspension more homogeneous **(Supplementary Fig. 2a)**. The size of the aggregates was measured by dynamic light scattering method using Zetasizer Nano ZS (Malvern Panalytical Ltd, Malvern, United Kingdom). Following sonication, the suspension was left overnight to sediment. After sedimentation, around 80% of supernatant (clear TGME solvent) volume was removed, and the remaining slurry was stirred and loaded into the barrel of the ink-jet printing head. To evaluate the stability of the jetting process, we measured average drop volume and platinum content at regular time intervals after loading the ink. The valve was operated with a 100 µs opening time without applying external pressure to produce a steady jet of droplets. At each time point, 5 000 drops were produced and the average drop volume and dry platinum content were measured **(Supplementary Fig. 2b)**. The drop size and platinum content initially increase, but reach a plateau of stable droplet output probably due to settlement of platinum particles in the valve. Printing was performed more than 2 hours after ink loading, when the drop size and platinum content stabilized. When the depletion of platinum content was observed, new ink was loaded.

Array Printing Process. *G-code preparation***.** Design of the models for printing was done directly in G-code using a custom-developed python program. It provided high flexibility in tuning printing parameters for each particular feature of the design as well as create designs where printing is done not only in xy plane layer by layer but also in the direction of z axis (for example to correct the tilt of the substrate).
Substrate preparation. Printing was done on standard glass slides (75x25x1 mm). The slide was treated with plasma using Piezobrush® PZ2-i installed in the printer (feed rate was 5 mm/s, distance between lines was 5 mm, distance between the substrate and the plasma adapter was approximately 5 mm). Then, it was left in 2% solution of sodium dodecyl sulfate (SDS) for at least 15 min, then dried with air stream. SDS treatment creates a layer of detergent molecules on the surface which prevents permanent adhesion of the silicone to glass.
Printing base layer and walls ***(Fig. 2a, panels i – iii).*** The base layer of the implants was printed using a 110 µm needle with SE1700 silicone. The applied back pressure and feed rate as well as distance from the nozzle to the substrate were adjusted according to the extrusion speed of the silicone which is slowly changed with time due to limited “pot life” as discussed in our previous publication (50). Empty spaces (vias) were left while printing this layer, in order to form the openings of the electrodes. The resolution with which such openings can be patterned is illustrated in **Supplementary Fig. 5a.**
After printing the base layer, the sample was transferred onto a hotplate and baked at 120°C for approximately 3 min. After transferring back to the printer the sample was treated with plasma (the same parameters as for glass slide treatment). Walls of SE1700 silicone were then printed to delineate the borders within which the conductive ink should be deposited.
Printing suspension inks ***(Fig. 2a, panel iv).*** As the next step, platinum suspension was deposited using ink jet method into grooves formed by the silicone walls. The valve was operated with the 100 µs opening time without applying backpressure. The printing was done with 5-10 mm/s feed rates and the interval between drops of around 100 µm. Plasma activation (performed at the previous step) enhances wettability of the surface and facilitates the spreading of the ink in the area limited by the less hydrophilic walls. The improvement of the resolution introduced by printed silicone walls is illustrated in **Supplementary Fig. 5b,c**. After ink jet printing, the sample was transferred onto a hotplate again to evaporate the TGME solvent (120°C for 5 min) to leave only dry platinum particles in the grooves. Printing and drying was repeated until a continuous film of platinum microparticles is formed inside the space defined by the borders. This typically requires two or three print runs. Printing of AgNW suspensions followed a similar procedure. Silver nanowire suspension in water was obtained from Sigma (806609-25ML). The nanowire concentration is 5mg/ml. According to the manufacturer: Wire diameter, D = 20±2 nm, and length L = 12±2 µm. The suspension was shaken up and directly loaded into the valve.
Connector Assembly ***(Fig. 2a, panel v).*** To establish electrical connection, the printed portion of the implant was attached to thin, Teflon coated stainless steel wires (Science Products, 7SS-2T). Separation compartments were printed at the ends of platinum interconnects using the SE1700 silicone. The compartments were filled with a conductive epoxy paste (Epo-Tek H27D, part A) via nozzle extrusion. The stripped ends of stainless steel wires were then embedded in the conductive epoxy providing mechanically adaptive electrical contact. To obtain extrudable consistency, the conductive epoxy was mixed with ethanol and printed via conical needles with the 410 µm inner tip diameter. After this procedure samples were left in the oven for 2 h at 80°C, to evaporate ethanol from the silver paste ink. On the opposite ends, stainless steel wires were attached to an Omnetics 12 pin male circular connector (A22017-001).
Implant sealing ***(Figure 2a, panel vi and vii).*** A final sealing layer was formed on top of the implant by dispensing Sylgard 184 via a 150 µm inner diameter cylindrical nozzle. This type of silicone (PDMS), having low surface tension, flows in between previously patterned platinum particles filling all the empty space down to the base layer. A final polymerization step was performed in an oven at 90 °C for 2 h. The connector assembly was additionally reinforced by applying a thick layer of the clear silicone DC 734 (Dow Corning).
Finally, implants were carefully peeled from the substrate with tweezers and washed with ethanol.

In some cases, the electrodes openings would be covered with a thin layer of silicone, which had to be removed in a post-processing step. This layer was removed by polishing electrode sites under a stereo-microscope with a sharpened toothpick and applying diamond polishing paste (Kemet 3-W-C3).
Finished devices were exposed to air plasma (2 min, 80% power, ATTO plasma cleaner, Diener electronic) in order to improve their surface wettability. The time between plasma exposure and implant use was not controlled (typically several days), however we did not experience any issues relating to tissue adhesion or stabilization during implantation.

Characterization of NeuroPrint electrode arrays. *Impedance spectroscopy.* Measurements were performed using a potentiostat equipped with a frequency response analyser (AUTOLAB PGSTAT204 with FRA32M module, Metrohm). The impedance of printed electrodes was measured in phosphate-buffered saline (PBS) using a coiled platinum wire as a counter electrode and an Ag/AgCl wire as reference electrode. Impedance was measured at the open circuit potential, with excitation amplitude of 10 mV (pp).
Cyclic voltammetry. The cyclic voltammogramms were obtained using the same potentiostat in 300 mM solution of sulfuric acid at a scan rate of 1 V/s, as described previously (51). A coiled platinum wire was used as a counter electrode and a Ag/AgCl electrode with Double-Junction System (Metrohm AG) was used as reference.
Determination of charge injection capacity. Charge injection capacity is a measure of the maximum charge per unit area an electrode coating can deliver, without electrode polarization exceeding the water window. For its determination, printed electrodes were immersed in PBS and cathodic-first, biphasic current pulses (200 µs per phase) were passed between the electrode and a large platinum counter electrode. Current pulses were generated with AUTOLAB PGSTAT204 (Metrohm AG), and the electrode polarization (vs. Ag/AgCl reference electrode) was recorded on an oscilloscope (DSO-1084E Digital Storage Oscilloscope, Voltcraft). The amplitude of the current pulses was gradually increased until the electrode under test was polarized just outside the water window (-0.6 V to 0.8 V). The instantaneous polarization of the electrodes due to Ohmic resistances in the circuit was subtracted from voltage traces. The stability of electrodes under conditions of continuous stimulation was evaluated using trains of bi-phasic, charge balanced pulses (phase duration 200 µs, amplitude 100 µA, frequency 500 pulses/s) (5).
Stretching apparatus. For dry dynamic stretch measurements **(Fig. 2c, d)**, a Dynamic Mechanical Analysis (DMA) tester (SHIMADZU, EZ-SX) was used. In this instrument, clamps are vertically arranged with the lower clamp being stationary. For monitoring resistance during stretch **(Supplementary Fig. 4)**, simple straight conductive lines were printed and connectorized in the same way as the implants. The ends of conductors were secured in the stretcher clamps and the resistance change was monitored using a multimeter. Initial gauge lengths strain rates are indicated in the relevant figure captions. For wet static measurements under tensile strain **(Fig. 3a,c)**, implants were stretched and affixed to glass slides. The glass slides with the attached implant and a reference and counter electrodes were then easily immersed in electrolyte. For wet dynamic stretch measurements requiring electrolyte immersion **(Fig. 3b,d)** a custom setup was constructed. Briefly, a vessel was attached to the stationary clamp of the DMA and one end of the implant was glued to the bottom of the vessel. The free end of the implant (containing wire connections) was then attached to the moving clamp. When the vessel is filled with PBS electrolyte, electrodes are fully submerged. Counter and reference electrodes are also submerged in the vessel. In cyclic stretch experiments, initial gauge length and strain rate were as described above.
Electron microscopy. Cross sections of electrode arrays were prepared manually using a razor blade under a stereomicroscope. Imaging was performed on a JEOL JSM-7500F Field Emission Scanning Electron Microscope. Prior to imaging, a thin layer of platinum was sputtered on the sample under investigation.

***In-vivo* experimental models and methods.** To test the capacities of the NeuroPrint technology to stimulate and record signals in different biological and histological environments we used the numbers of the experimental models and tissues with various electrical and mechanical properties (**Figs. 4-7**). Accordingly, the specific designs of the electrode interfaces were fabricated on-demand for the experimental task and animal model (**Supplementary Fig. 11**). All procedures were conducted in accordance with a protocol approved by the Animal Care Committee of the Pavlov Institute of Physiology, St. Petersburg, Russia, and followed the European Community Council Directive (2010/63EU) and the guidelines of the National Institute of Health Guide for the Care and Use of Laboratory Animals.
Decerebrated cat model. We first performed experiments on decerebrated cat model. This unique motor impaired *in vivo* model has contributed markedly to studying sensorimotor control (52), developing methods of the brain stem (53, 54) and the spinal cord stimulation (55, 56), as well as to triggering capacities of distributed spinal networks (57). This model has also been critical for understanding mechanisms of the regulation of various other physiological functions, including the urinary system activity (58, 59) in non-anesthetized animals without voluntary control and forebrain input.
Experiments were performed on 8 adult cats of either sex (weighing 2.5–3.5 kg). The cats were anesthetized deeply with isoflurane (2–4%) delivered in O_2. The level of anesthesia was monitored by applying pressure to a paw (to detect limb withdrawal), as well as by checking the size and reactivity of pupils. The trachea was

cannulated and carotid arteries were ligated. The animals were decerebrated at the precollicular-postmammillary level (37).
A laminectomy was performed in the lumbar-sacral area to access S1-S3 spinal segments (**Fig. 4b**) for subdural implantation of spinal NeuroPrint electrode array (**Supplementary Fig. 11**). The sciatic nerve was exposed proximally on the hip close to pelvis to implant NeuroPrint electrodes for nerve stimulation. The pairs of the single EMG NeuroPrint electrodes and stainless steel Teflon-insulated wires (AS632; Cooner Wire) were implanted bilaterally into m. gastrocnemius lateralis (ankle extensor) and m. iliopsoas (hip flexor) as described previously (60).
Anesthesia was discontinued after the surgical procedures, and the experiments were started 2–3 h thereafter. During the experiment, the rectal temperature, electrocardiography, and breathing rate of the animal were continuously monitored. They were kept at 37 ± 0.5°C, 110–140 beats/min, and 20–40 breaths/min, respectively.
The head of the decerebrated animal, the vertebral column, and the pelvis were fixed in a rigid frame (32). The hindlimbs were positioned on the treadmill. The distance between the treadmill belt and the fixed pelvis was 21–25 cm (depending on the animal's size), which determined a limb configuration similar to that observed in the intact cat in the middle of stance during walking. The cats decerebrated at the precollicular-postmammillary level are motor impaired and not normally able for spontaneous locomotor activity (**Fig. 4c**). Locomotion was evoked by electrical spinal cord stimulation (**Fig. 4b**) using NeuroPrint electrode array (S1-S3 segments; 5 Hz; 0.2–0.5 ms; 80–200 μA) or by mesencephalic locomotor region stimulation (Horsley-Clark coordinates P2, R/L4, H0; 30 Hz; 1 ms; 50–200 μA) (37). In the latter case, the lumbosacral multi-electrode array was used for monitoring of the spinal locomotor network (**Supplementary Fig. 12**). The gait-modulated ElectroSpinoGram (ESG) was recorded during brain-stem evoked walking of decerebrated cat (**Supplementary Fig. 12a,b**). The electrode and time averaged power spectrum density was significantly higher during stepping *vs* standing of the animal (**Supplementary Fig. 12c,d**). To define the exact location of spinal NeuroPrint electrode array and rostrocaudal ES stimulation points a thorough dissection of the spinal cord was performed at the end of each experiment.
To characterize kinematics of locomotor movements, reflective markers were placed on the iliac crest, femoral head, lateral condyle of the femur, lateral malleolus, fifth metatarsal joint, and video (25 frames/s) of the side view of the walking cat was recorded (**Fig. 4a,c**). In addition, we recorded the anterior–posterior (A–P) limb movements by means of 2 mechanical sensors (synchronized with EMG, ESG and video recordings). The signals from the EMG electrodes and from the position sensors were amplified (bandwidth 30–500 Hz), digitized at 2 kHz, and saved to a computer disk.
Urodynamic study and recording of cat smooth detrusor muscles activity. The intravesical pressure (**Fig. 5f**) was measured using a cystometry sensor (61). Following a midline abdominal incision, a catheter (Perifix 401, 18G) was introduced through the apex of the bladder and secured using a 6.0 Ethilon suture (Ethicon, New Brunswick, NJ). The catheter was connected to a solid-state pressure transducer (MLT0670, AU) and through a syringe pump (ZOOMED SN-1600 V, RU), 0.9% saline solution (at room temperature) was injected. Bipolar NeuroPrint EMG electrodes **(Supplementary Fig. 11, Fig. 1b *iv*)** were implanted in smooth detrusor muscle. The EMG signal was differentially amplified (A-M Systems USA, model 1700, bandwidth of 10 Hz-5 kHz), digitized at 20 kHz with a National Instrument A/D board, rectified, and integrated by computer programs. EMG activity of the detrusor smooth muscle signal was filtered at 10–40 Hz (38). The flow rate was calculated as the smoothed derivative (over 15-s windows) of the volume of the urine (raw signal recorded and digitized at 5 kHz).
Accessing the swimming network in the zebrafish model. The study was performed in adult (5-7 months) wild-type short-fin zebrafish (n=5) obtained from a commercial vendor (Tropical Aquarium, St. Petersburg, Russia). Animal housing adhered to the accepted standards of zebrafish care. Animals were kept in 20-L tank with water filtration system, water temperature set at 25 °C, light at 950-960 lux, with 10/14-hours cycle of day/night (61). Behavioral and neurophysiological testing was performed in the novel tank test, representing a plexiglass container (20 x 20 x 5 cm). Prior to testing, the animals were quickly anaesthetized by buffered tricaine methanesulfonate (MS-222) (62), and sets of bipolar fish NeuroPrint electrodes **(Supplementary Fig. 11, Fig. 1b *iv*)** were implanted into the dorsal muscles of opposing sides of the same segment or into more rostral and caudal muscle on the same side (39). Spontaneous bouts of swimming were recorded, as were bouts elicited by gently touching the fish around the tail or electrical stimulation of the back by way the NeuroPrint implants positioned just above the spinal cord on the mid-abdominal level. Individual bouts occurred when the fish swam actively. Each bout consisted of several bursts of EMG activity, each comprised of several EMG spikes (**Fig. 5g**). We also video-recorded fish movements utilizing the top- and side-view cameras, to further analyze offline the kinematics of their swimming synchronously to the EMG signals.
Chronically implanted rat model. Evaluation of the long-term biointegration and functionality of NeuroPrint technology was carried out on the chronically implanted rat model (Wistar male rats 3-6 months, 350-420 g). 1st and 2nd groups *of rats*: In the biocompatibility study, rats received either a sham (1st group, n=4), or spinal NeuroPrint (2nd group, n=4) implant, with bipolar electrodes inserted into the ankle muscles to record electromyographic (EMG) activity. Prior to surgery, rats were handled and trained daily in the locomotor tasks for three weeks, including walking on the runway, treadmill with different speeds, and crossing a horizontal

ladder. Prior to the training, rats underwent a mild food deprivation and were rewarded with yoghurt at the end of each trial. The body weight was monitored closely, and in case of weight loss, the food deprivation was properly adjusted. The impedance testing of the NeuroPrint electrode arrays and their functional capacities for different applications were performed every week. The animals were tested for motor impairment and fine aspect of locomotor and postural abilities and then euthanized 8 weeks post-implantation, for histological evaluation of neuroinflammation in the lumbar spinal cord. 3rd group: Recording of electrocorticograms, somatosensory and motor evoked potentials were performed in rats (n = 4) implanted with NeuroPrint arrays **(Supplementary Fig. 11, Fig. 1b *i*)** over the leg area of the motor cortex, and with bipolar electrodes into ankle muscles of both legs. These rats underwent the same behavioral training as rats in the biocompatibility group (above).

Implantation of NeuroPrint array into the spinal subdural space. The rat spinal NeuroPrint arrays were implanted under Isoflurane/Dorbene anesthesia **(Supplementary Fig. 11, Fig. 1b *ii*)**. Under sterile conditions, a dorsal midline skin incision was made and the muscles covering the dorsal vertebral column were removed. A partial laminectomy was performed at vertebrae levels L3-L4 and T12-T13 to create entry and exit points for the implant. To access the intrathecal space, a 3mm long mediolateral incision was performed in the dura mater at both laminectomy sites. A loop of surgical suture (Ethilon 4.0) was inserted through the rostral (T12-T13) dura mater incision and pushed horizontally along the subdural space until the loop emerged through the caudal (L3-L4) dura mater incision. The extremity of the implant was then folded around the suture loop. The loop was then retracted gently to position the implant over the spinal cord. A small portion of the implant protruded beyond the rostral dura mater incision and could be manipulated with fine forceps to adjust the mediolateral and rostrocaudal positioning of the implant. Electrophysiological testing was performed intra-operatively to fine-tune positioning of electrodes with respect to lumbar and sacral segments (34). The protruding extremity of the implant became encapsulated within connective tissues, which secured positioning of the implant in the chronic stages. The soft-to-wires connector was secured to the bone using a newly developed vertebral orthosis (63). The connector was first positioned above the vertebral bone. Four micro-screws (Precision Stainless Steel 303 Machine Screw, Binding Head, Slotted Drive, ANSI B18.6.3, #000-120, 0.125) were inserted into the bone of rostral and caudal vertebrae. Surgical suture (Ethilon 4.0) was used to form a cage around the micro-screws and connector. The walls of the cage were plastered using freshly mixed dental cement (ProBase Cold, Ivoclar Vivadent) extruded through a syringe. After solidification of the dental cement, the electrical wires were routed subcutaneously to the head of the rat, where an Omnetics electrical connector was secured to the skull using dental cement. The same method was used to create the vertebral orthosis for sham implants in the biocompatibility study.

Implantation of NeuroPrint into the cortical subdural space. The rat cortex NeuroPrint arrays **(Supplementary Fig. 11, Fig. 1b *i*)** were implanted under Isoflurane/Dorbene anesthesia. Under sterile conditions, 2 trepanations were performed on the right half of the skull to create two windows rostral and caudal to the leg area of the motor cortex. The first window was located cranially with respect to the coronal suture, while the second window was located cranially with respect to the interparietal suture. Both windows were located close to the sagittal suture in order to position the center of the NeuroPrint electrodes 1 mm lateral and 1mm caudal relative to the bregma. The surgical insertion technique developed for passing arrays into the spinal subdural space was also used for implantation into the cortical subdural space. Excess implant length was cut in the cranial window, and the edge of the implants sutured to the dura mater using a Ethilon 8.0 suture. The exposed parts of the brain and external part of the NeuroPrint array were covered with surgical silicone (KWIK-SIL). A total of 4 screws were implanted into the skull around the NeuroPrint connector before covering the entire device, the connector, and the percutaneous amphenol connector with dental cement.

Implantation of electrodes to record muscle activity. All the procedures have been reported in details previously (63). Briefly, bipolar intramuscular electrodes (AS632; Cooner Wire) were implanted into the tibialis anterior and medial gastrocnemius muscles, bilaterally. Recording electrodes were fabricated by removing a small part (1mm notch) of insulation from each wire. A common ground wire (1cm of Teflon removed at the distal end) was inserted subcutaneously over the right shoulder. All electrode wires were connected to a percutaneous amphenol connector (Omnetics Connector Corporation) cemented to the skull of the rat. The proper location of EMG electrodes was verified post-mortem.

Histological evaluation of the biointegration of the NeuroPrint electrode arrays

Immunohistochemical protocol. Since persistent neuroinflammation after implantation involves microglial activation (64), we used an iba-1 marker (**Fig. 6e**) recognizing microglial cells for the histological biocompatibility assessment. The detailed procedure of immunohistochemical staining was described previously (65). After deparaffinization, temperature unmasking and endogenous peroxidase activity blocking, sections were preincubated with 5% bovine serum albumin (BSA) (Vector Laboratories, UK), followed by incubation for 18 hours in a polyclonal rabbit primary antibody against ionized calcium binding adapter molecule 1 (Iba-1), (Abcam Cat# ab5076, RRID: AB_2224402, 1:300 dilution). Then, slices were incubated in a LSAB+ (Dako, Denmark). Thereafter, slices were processed in DAB+ kit (Dako, Denmark). Slices were coverslipped in Canadian balsam and after drying, were analyzed with an Olympus microscope (Olympus Corporation, Japan) using a Nikon camera (Nikon Corporation, Japan).

Image analysis. Four representative slices of the lumbar segment L3 were used for every rat. Glial immunoreaction was analyzed in two ways: (1) by semi-automatic assessment of the relative optical density and relative area of the glia-containing regions, and (2) by the manual estimation of the total number of glial cells, using open-source software from Fiji (PRID: SCR_002285) (66). In the former case, all images were pre-processed, contrasted and filtered in the same way. Thereafter, the optical density and the area of the pixels having darkness level under the defined level, were assessed; these values were divided onto the optical density / pixels area of the total slice of the spinal cord using Michelson contrast to assess a signal visibility (**Fig. 6f**). The Michelson contrast is defined as $(I_{max}-I_{min})/(I_{max}+I_{min})$, where I_{max} and I_{min} are the highest and lowest luminance. In our case, I_{max} was a signal (brightness of the glial somas), and I_{min} was a background. In the case of the manual estimation of the number of glial cells, only glial cells having soma, but not separate glial processes were counted (**Fig. 6e**). It was shown that during activation, microglia undergo particular morphological alterations changing themselves from a ramified structure (so-called "resting glia") to rather amoeboid cells (41, 67). Therefore, for more detailed analysis, microglial cells were related to the following types: type 1 cells had thin processes and small soma; type 2 cells had thick processes and large soma; the first type was related to the resting glia, and the second type – to the activated glia following criteria previously elaborated (40, 68). In these analyses, 4 slices from every animal were used. Data presented as mean±SD. Statistical differences were assessed using the nested t-test.
In all slices independently of the group, the Iba-1-immunopositive glial cells were detected in both white and gray matter (see a representative example in **Fig. 6e**). A population of the glial cells *per* slice was variable, and their total amount was assessed using both semi-automatic and manual ways. In the first case, a relative optical density and a relative area of the glia-containing regions were assessed, with no statistical differences found between SHAM and SUB groups (relative area: -0.9797 ± 0.0145 *vs* -0.9858 ± 0.0083, t=0.9476, df=30, p=0.3509); relative optical density: -0,1381± 0.0292 *vs* -0,1637± 0.0294, t=1.395, df=6, p=0.2124). Manual counting of the glial cells also did not reveal any differences between these two groups (854 ± 650 *vs* 880 ± 307, t=0.1038, df=14, p=0.9188) (**Fig. 6e,f**). Counting of different cell types (see above) revealed that most glial cells in Sham and SUB groups were resting glia (74.44 ± 19.9 % *vs* 80.93 ± 8.5 %, t=0.8451, df=14, p=0.4122), and minor amount were activated glial cells (25.56 ± 19.9 % *vs* 19.07 ± 8.5 %, t=0.8451, df=14, p=0.4122). The distribution of these cells is presented at **Suppl. Fig. 13.**

Neurophysiological recording to test functional stability of the NeuroPrint electrode arrays.
*Chronic recordings of the fine features of the locomotor and postural control (***Fig. 6j-q, Supplementary Fig. 14, 15***).*To evaluate biocompatibility of the NeuroPrint technology, the detailed kinematic analysis of the sham and implanted rats stepping on the runway and treadmill was done. The video recordings from the side, back views and below the animal ("foot print" test) were quantified and used for analysis of multiple characteristics including timing of the step cycle, step width, length and height, mediolateral displacement of the body center of mass , lateral foot placement, interlimb coordination and reproducibility of the locomotor activity.
Chronic recordings of ESG (**Fig. 7d, Supplementary Fig. 16**). Recordings of electrical potentials from the electrodes integrated in the chronically implanted NeuroPrint array, which we called electrospinograms, were performed after 8 weeks of implantation (n=4). Signals were recorded using an Intan Stimulation/Recording controller based on RHS2116 chips with a sampling frequency 20 kHz and digital band-pass filter (0,1...6000 Hz). ESGs were recorded differentially from each active site of the implants with respect to a reference fixed to one of the bony vertebrae. The amplitude, and power spectrum density, of the recorded signals were analyzed offline.
Site-specific stimulation of the spinal cord (**Fig. 7e, Supplementary Fig. 17**).To test the stimulating capacity of NeuroPrint arrays after chronic (8-week) implantation, the electrical stimulation of the rat spinal cord was applied in four different locations: left rostral, right rostral, left caudal and right caudal (n=4). EMG activity (**Fig. 7e)** and kinematics (**Supplementary Fig. 17**) in different joints were recorded to find out the site-specificity of the stimuli. Subdural electrical stimulation currents were delivered between active electrodes located on the lateral aspect or midline of sacral (S1) and lumbar (L3) segments, and an indifferent ground located subcutaneously. The intensity of electrical spinal cord stimulation was tuned (1 Hz, 20-150 μA, biphasic rectangular pulses, 0.2 ms duration).
Long-term in vivo recordings of electrocorticograms in freely behaving rats (**Fig. 7f-h, Supplementary Fig. 18**). Electrocorticograms (ECoG)s were measured in conjunction with whole body kinematics and muscle activity recordings during standing and walking in freely behaving rats (n=5 rats) **(Supplementary Fig. 18)**. A lateral active site integrated in the NeuroPrint was used as a reference for differential amplification. A wire ground was fixed to the skull using a metallic screw. Differential recordings were obtained using an Intan Stimulation / Recording controller based on RHS2116 chips with a sampling frequency 20 kHz and digital band-pass filter (0,1...6000 Hz). Raw electrocorticograms were elaborated using previously described methods (Pistohl et al. 2012). Kinematic and muscle activity recordings were used to dissociate standing and walking states (**Supplementary Fig. 18**). Motor evoked potentials in the hindlimb muscle bilaterally were induced by cortex NeuroPrint stimulation, located in motor region of hindlimb (burst: biphasic, 0.5 ms duration, 333 Hz impulse 1.1 mA; the repetition rate of the burst is 15 s) **(Fig. 7f,h)**. Somatosensory evoked potential was

recorded by cortex NeuroPrint array during stimulation of the ipsi- and contralateral gastrocnemius medialis muscle (single 0.5 ms duration 1 Hz, 100 stimulus, 300-700 µA matched to functional response) **(Fig. 7f,g)**. *Statistical analysis.* Unless stated otherwise, data are presented as mean±SE. Statistical evaluations were performed using Student's t-test (as for paired as for unpaired normally distributed samples) or using Mann-Whitney test otherwise at the p=0.05 level of significance. Pearson correlation coefficients were used to determine the relationships between pairs of variables. The Fourier transformation of ESG and ECoG signals was performed. The z-score normalized time resolved power spectral densities (trPSD) averaged across all electrodes is shown in units of standard deviation (SD). The spectrum was divided to low frequency band (LFB, 2-25 Hz) and high frequency band (HFB, 75-300 Hz) to remove the effect of the 50-Hz line noise. The mean power spectrum density was calculated for each frequency band (5, 69).

Reporting summary. Further information on research design is available in the Nature Research Reporting Summary linked to this article.

Data availability

The main data supporting the results in this study are available within the paper and its Supplementary Information. The raw and analysed datasets generated during the study are too large to be publicly shared, yet they are available for research purposes from the corresponding authors on reasonable request.

Code availability

The code used to program the printer paths can be found here: https://sourceforge.net/projects/g-code-processor/

References

1 Wagner, F. B. *et al.* Targeted neurotechnology restores walking in humans with spinal cord injury. *Nature* **563**, 65-71, doi:10.1038/s41586-018-0649-2 (2018).

2 Granata, G. *et al.* Phantom somatosensory evoked potentials following selective intraneural electrical stimulation in two amputees. *Clinical Neurophysiology* **129**, 1117-1120, doi:https://doi.org/10.1016/j.clinph.2018.02.138 (2018).

3 Ajiboye, A. B. *et al.* Restoration of reaching and grasping movements through brain-controlled muscle stimulation in a person with tetraplegia: a proof-of-concept demonstration. *The Lancet* **389**, 1821-1830 (2017).

4 Liu, Y. *et al.* Soft and elastic hydrogel-based microelectronics for localized low-voltage neuromodulation. *Nature Biomedical Engineering* **3**, 58-68, doi:10.1038/s41551-018-0335-6 (2019).

5 Minev, I. R. *et al.* Electronic dura mater for long-term multimodal neural interfaces. *Science* **347**, 159-163, doi:10.1126/science.1260318 (2015).

6 Fu, T.-M., Hong, G., Viveros, R. D., Zhou, T. & Lieber, C. M. Highly scalable multichannel mesh electronics for stable chronic brain electrophysiology. *Proceedings of the National Academy of Sciences* **114**, E10046-E10055, doi:10.1073/pnas.1717695114 (2017).

7 Boutry, C. M. *et al.* A stretchable and biodegradable strain and pressure sensor for orthopaedic application. *Nature Electronics* **1**, 314-321, doi:10.1038/s41928-018-0071-7 (2018).

8 Kim, T.-i. *et al.* Injectable, Cellular-Scale Optoelectronics with Applications for Wireless Optogenetics. *Science* **340**, 211-216, doi:10.1126/science.1232437 (2013).

9 Reeder, J. *et al.* Mechanically Adaptive Organic Transistors for Implantable Electronics. *Advanced Materials* **26**, 4967-4973, doi:10.1002/adma.201400420 (2014).

10 Lu, C. *et al.* Flexible and stretchable nanowire-coated fibers for optoelectronic probing of spinal cord circuits. *Science Advances* **3**, doi:10.1126/sciadv.1600955 (2017).

11 Sengeh, D. M. & Herr, H. A variable-impedance prosthetic socket for a transtibial amputee designed from magnetic resonance imaging data. *JPO: Journal of Prosthetics and Orthotics* **25**, 129-137 (2013).

12 Filardo, G. *et al.* Novel alginate biphasic scaffold for osteochondral regeneration: an in vivo evaluation in rabbit and sheep models. *Journal of Materials Science: Materials in Medicine* **29**, 74, doi:10.1007/s10856-018-6074-0 (2018).

13 Ploch, C. C., Mansi, C. S., Jayamohan, J. & Kuhl, E. Using 3D printing to create personalized brain models for neurosurgical training and preoperative planning. *World neurosurgery* **90**, 668-674 (2016).

14 Valentine, A. D. *et al.* Hybrid 3D Printing of Soft Electronics. *Advanced Materials* **29**, 1703817-n/a, doi:10.1002/adma.201703817 (2017).

15 Lind, J. U. *et al.* Instrumented cardiac microphysiological devices via multimaterial three-dimensional printing. *Nat Mater* **16**, 303-308, doi:10.1038/nmat4782

http://www.nature.com/nmat/journal/v16/n3/abs/nmat4782.html#supplementary-information (2017).
16 Bachmann, B. *et al.* All-inkjet-printed gold microelectrode arrays for extracellular recording of action potentials. *Flexible and Printed Electronics* **2**, 035003 (2017).
17 Markos Athanasiadis *et al.* Printed elastic membranes for multimodal pacing and recording of human stem-cell-derived cardiomyocytes *npj Flexible Electronics* **xxx**, xxx, doi: https://doi.org/10.1038/s41528-020-0075-z (2020).
18 Minev, I. R., Wenger, N., Courtine, G. & Lacour, S. P. Research Update: Platinum-elastomer mesocomposite as neural electrode coating. *APL Materials* **3**, -, doi:doi:http://dx.doi.org/10.1063/1.4906502 (2015).
19 Mo, L. *et al.* Nano-Silver Ink of High Conductivity and Low Sintering Temperature for Paper Electronics. *Nanoscale Research Letters* **14**, 197, doi:10.1186/s11671-019-3011-1 (2019).
20 van Noort, R., Black, M. M., Martin, T. R. P. & Meanley, S. A study of the uniaxial mechanical properties of human dura mater preserved in glycerol. *Biomaterials* **2**, 41-45, doi:https://doi.org/10.1016/0142-9612(81)90086-7 (1981).
21 Kwan, M. K., Wall, E. J., Massie, J. & Garfin, S. R. Strain, stress and stretch of peripheral nerve Rabbit experiments in vitro and in vivo. *Acta Orthopaedica Scandinavica* **63**, 267-272, doi:10.3109/17453679209154780 (1992).
22 Calvo, B. *et al.* Passive nonlinear elastic behaviour of skeletal muscle: Experimental results and model formulation. *Journal of Biomechanics* **43**, 318-325, doi:https://doi.org/10.1016/j.jbiomech.2009.08.032 (2010).
23 Nicholson, K. J. & Winkelstein, B. A. in *Neural Tissue Biomechanics* (ed Lynne E. Bilston) 203-229 (Springer Berlin Heidelberg, 2011).
24 Harrison, D. E., Cailliet, R., Harrison, D. D., Troyanovich, S. J. & Harrison, S. O. A review of biomechanics of the central nervous system—Part II: Spinal cord strains from postural loads. *Journal of Manipulative and Physiological Therapeutics* **22**, 322-332, doi:http://dx.doi.org/10.1016/S0161-4754(99)70065-5 (1999).
25 Diani, J., Fayolle, B. & Gilormini, P. A review on the Mullins effect. *European Polymer Journal* **45**, 601-612, doi:https://doi.org/10.1016/j.eurpolymj.2008.11.017 (2009).
26 Neto, J. P. *et al.* Does Impedance Matter When Recording Spikes With Polytrodes? **12**, doi:10.3389/fnins.2018.00715 (2018).
27 Cogan, S. F. Neural Stimulation and Recording Electrodes. *Annual Review of Biomedical Engineering* **10**, 275-309, doi:doi:10.1146/annurev.bioeng.10.061807.160518 (2008).
28 Biegler, T. An Electrochemical and Electron Microscopic Study of Activation and Roughening of Platinum Electrodes. *Journal of The Electrochemical Society* **116**, 1131, doi:10.1149/1.2412234 (1969).
29 Tondera, C. *et al.* Highly Conductive, Stretchable, and Cell-Adhesive Hydrogel by Nanoclay Doping. *Small* **0**, 1901406, doi:10.1002/smll.201901406 (2019).
30 Won, S. M. *et al.* Recent Advances in Materials, Devices, and Systems for Neural Interfaces. **30**, 1800534, doi:10.1002/adma.201800534 (2018).
31 Capogrosso, M. *et al.* A brain–spine interface alleviating gait deficits after spinal cord injury in primates. *Nature* **539**, 284-288, doi:10.1038/nature20118 (2016).
32 Musienko, P. E. *et al.* Spinal and Supraspinal Control of the Direction of Stepping during Locomotion. *The Journal of Neuroscience* **32**, 17442-17453, doi:10.1523/jneurosci.3757-12.2012 (2012).
33 Harkema, S. *et al.* Effect of epidural stimulation of the lumbosacral spinal cord on voluntary movement, standing, and assisted stepping after motor complete paraplegia: a case study. *The Lancet* **377**, 1938-1947, doi:http://dx.doi.org/10.1016/S0140-6736(11)60547-3 (2011).
34 Courtine, G. *et al.* Transformation of nonfunctional spinal circuits into functional states after the loss of brain input. *Nat Neurosci* **12**, 1333-1342 (2009).
35 Wenger, N. *et al.* Spatiotemporal neuromodulation therapies engaging muscle synergies improve motor control after spinal cord injury. *Nat Med* **22**, 138-145, doi:10.1038/nm.4025 http://www.nature.com/nm/journal/v22/n2/abs/nm.4025.html#supplementary-information (2016).
36 Hoffman, P. Beitrage zur Kenntnis der menschlichen Reflexe mit besonderer Berucksichtigung der elektrischen Erscheinungen. *Arch F Physiol*, 223-256 (1910).
37 Shik, M. L. Control of walking and running by means of electrical stimulation of the midbrain. *Biophysics (in Russian)* **11**, 659-666 (1966).
38 Fry, C. H., Wu, C. & Sui, G. P. Electrophysiological properties of the bladder. *International Urogynecology Journal* **9**, 291-298, doi:10.1007/bf01901509 (1998).
39 Liu, D. W. & Westerfield, M. Function of identified motoneurones and co-ordination of primary and secondary motor systems during zebra fish swimming. *The Journal of Physiology* **403**, 73-89, doi:10.1113/jphysiol.1988.sp017239 (1988).
40 Hains, B. C. & Waxman, S. G. Activated Microglia Contribute to the Maintenance of Chronic Pain after Spinal Cord Injury. **26**, 4308-4317, doi:10.1523/JNEUROSCI.0003-06.2006 %J The Journal of Neuroscience (2006).
41 Sierra, A. *et al.* The “Big-Bang” for modern glial biology: Translation and comments on Pío del Río-Hortega 1919 series of papers on microglia. **64**, 1801-1840, doi:10.1002/glia.23046 (2016).

42 Musienko, P. *et al.* Somatosensory control of balance during locomotion in decerebrated cat. *Journal of Neurophysiology* **107**, 2072-2082, doi:10.1152/jn.00730.2011 (2012).
43 Nonnekes, J. *et al.* Neurological disorders of gait, balance and posture: a sign-based approach. *Nature Reviews Neurology* **14**, 183-189, doi:10.1038/nrneurol.2017.178 (2018).
44 Musienko, P. E. *et al.* [Neuronal control of posture and locomotion in decerebrated and spinalized animals]. *Ross Fiziol Zh Im I M Sechenova* **99**, 392-405 (2013).
45 Gill, M. L. *et al.* Neuromodulation of lumbosacral spinal networks enables independent stepping after complete paraplegia. *Nature Medicine*, doi:10.1038/s41591-018-0175-7 (2018).
46 Kim, Y. *et al.* A bioinspired flexible organic artificial afferent nerve. **360**, 998-1003, doi:10.1126/science.aao0098 %J Science (2018).
47 Vu, P. P. *et al.* A regenerative peripheral nerve interface allows real-time control of an artificial hand in upper limb amputees. **12**, eaay2857, doi:10.1126/scitranslmed.aay2857 %J Science Translational Medicine (2020).
48 Vachicouras, N. *et al.* Microstructured thin-film electrode technology enables proof of concept of scalable, soft auditory brainstem implants. **11**, eaax9487, doi:10.1126/scitranslmed.aax9487 %J Science Translational Medicine (2019).
49 Borton, D. *et al.* Corticospinal neuroprostheses to restore locomotion after spinal cord injury. *Neuroscience Research* **78**, 21-29, doi:http://dx.doi.org/10.1016/j.neures.2013.10.001 (2014).
50 Athanasiadis, M., Pak, A., Afanasenkau, D. & Minev, I. R. Direct Writing of Elastic Fibers with Optical, Electrical, and Microfluidic Functionality. *Advanced Materials Technologies* **4**, 1800659, doi:10.1002/admt.201800659 (2019).
51 Hudak, E. M., Mortimer, J. T. & Martin, H. B. Platinum for neural stimulation: voltammetry considerations. *Journal of Neural Engineering* **7**, 026005 (2010).
52 Whelan, P. J. CONTROL OF LOCOMOTION IN THE DECEREBRATE CAT. *Progress in Neurobiology* **49**, 481-515, doi:https://doi.org/10.1016/0301-0082(96)00028-7 (1996).
53 Shik, M. L. & Orlovsky, G. N. Neurophysiology of locomotor automatism. *Physiological Reviews* **56**, 465-501, doi:10.1152/physrev.1976.56.3.465 (1976).
54 Mori, S., Kawahara, K., Sakamoto, T., Aoki, M. & Tomiyama, T. Setting and resetting of level of postural muscle tone in decerebrate cat by stimulation of brain stem. *Journal of Neurophysiology* **48**, 737-748, doi:10.1152/jn.1982.48.3.737 (1982).
55 Iwahara, T., Atsuta, Y., Garcia-Rill, E. & Skinner, R. D. Spinal cord stimulation-induced locomotion in the adult cat. *Brain Research Bulletin* **28**, 99-105, doi:https://doi.org/10.1016/0361-9230(92)90235-P (1992).
56 Gerasimenko, Y. P. *et al.* Formation of locomotor patterns in decerebrate cats in conditions of epidural stimulation of the spinal cord. *Neuroscience and Behavioral Physiology* **35**, 291-298, doi:10.1007/s11055-005-0059-4 (2005).
57 Merkulyeva, N. *et al.* Activation of the spinal neuronal network responsible for visceral control during locomotion. *Experimental Neurology* **320**, 112986, doi:https://doi.org/10.1016/j.expneurol.2019.112986 (2019).
58 Kruse, M. N. & de Groat, W. C. Spinal pathways mediate coordinated bladder/urethral sphincter activity during reflex micturition in decerebrate and spinalized neonatal rats. *Neuroscience Letters* **152**, 141-144, doi:https://doi.org/10.1016/0304-3940(93)90503-D (1993).
59 Shefchyk, S. J. & Buss, R. R. Urethral pudendal afferent-evoked bladder and sphincter reflexes in decerebrate and acute spinal cats. *Neuroscience Letters* **244**, 137-140, doi:https://doi.org/10.1016/S0304-3940(98)00155-4 (1998).
60 Gerasimenko, Y. *et al.* Propriospinal Bypass of the Serotonergic System That Can Facilitate Stepping. *The Journal of Neuroscience* **29**, 5681-5689, doi:10.1523/jneurosci.6058-08.2009 (2009).
61 Westerfield, M. The Zebrafish Book : A Guide for the Laboratory Use of Zebrafish. *http://zfin.org/zf_info/zfbook/zfbk.html* (2000).
62 Martins, T., Valentim, A. M., Pereira, N. & Antunes, L. M. Anaesthesia and analgesia in laboratory adult zebrafish: a question of refinement. *Laboratory Animals* **50**, 476-488, doi:10.1177/0023677216670686 (2016).
63 Capogrosso, M. *et al.* Configuration of electrical spinal cord stimulation through real-time processing of gait kinematics. *Nature Protocols* **13**, 2031-2061, doi:10.1038/s41596-018-0030-9 (2018).
64 Jorfi, M., Skousen, J. L., Weder, C. & Capadona, J. R. Progress towards biocompatible intracortical microelectrodes for neural interfacing applications. *Journal of Neural Engineering* **12**, 011001, doi:10.1088/1741-2560/12/1/011001 (2014).
65 Kirik, O. V., Sukhorukova, E. G. & Korzhevskiĭ, D. E. Calcium-binding Iba-1/AIF-1 protein in rat brain cells. *Morfologiia* **137**, 5-8 (2010).
66 Schindelin, J. *et al.* Fiji: an open-source platform for biological-image analysis. *Nature Methods* **9**, 676, doi:10.1038/nmeth.2019
https://www.nature.com/articles/nmeth.2019#supplementary-information (2012).
67 Kreutzberg, G. W. Microglia: a sensor for pathological events in the CNS. *Trends in Neurosciences* **19**, 312-318, doi:https://doi.org/10.1016/0166-2236(96)10049-7 (1996).

68 Refolo, V. & Stefanova, N. Neuroinflammation and Glial Phenotypic Changes in Alpha-Synucleinopathies. **13**, doi:10.3389/fncel.2019.00263 (2019).
69 Pistohl, T., Schulze-Bonhage, A., Aertsen, A., Mehring, C. & Ball, T. Decoding natural grasp types from human ECoG. *NeuroImage* **59**, 248-260, doi:https://doi.org/10.1016/j.neuroimage.2011.06.084 (2012).

Acknowledgements

We acknowledge funding from the following sources: European Research Council (804005-IntegraBrain), St. Petersburg State University (project ID: 51134206 for OG and NM, animal facility and biocompatibility, validation of the implants on in-vivo models), Technische Universität Dresden, Russian Foundation for Basic Research (grant IDs: 20-015-00568-a for urodynamic study, 18-33-20062-mol_a_ved for developing optimal electrode array configuration), Deutsche Forschungsgemeinschaft (MI 2117/1-1), Volkswagen Foundation (Freigeist 91 690). We thank the following people for their help and expertise: Dr. D.E. Korzhevskiy (immunohistochemistry), Dr. Y.I. Sysoev (zebra fish model), A.V. Goriainova (functional tests), Thomas Kurth (electron microscopy).

Author contributions

I.R.M. and P.M. conceived and initiated the project and wrote the manuscript. D.A., D.K., O.G., N.P., I.R.M. and P.M. designed and performed experiments. D.A., D.K., V.L., C.T., S.M., N.M., A.V.K., I.R.M. and P.M. analysed data and contributed to writing the manuscript. P.M. and I.R.M. supervised the study.

Competing interests

The authors declare no competing interests.

Supplementary Figures

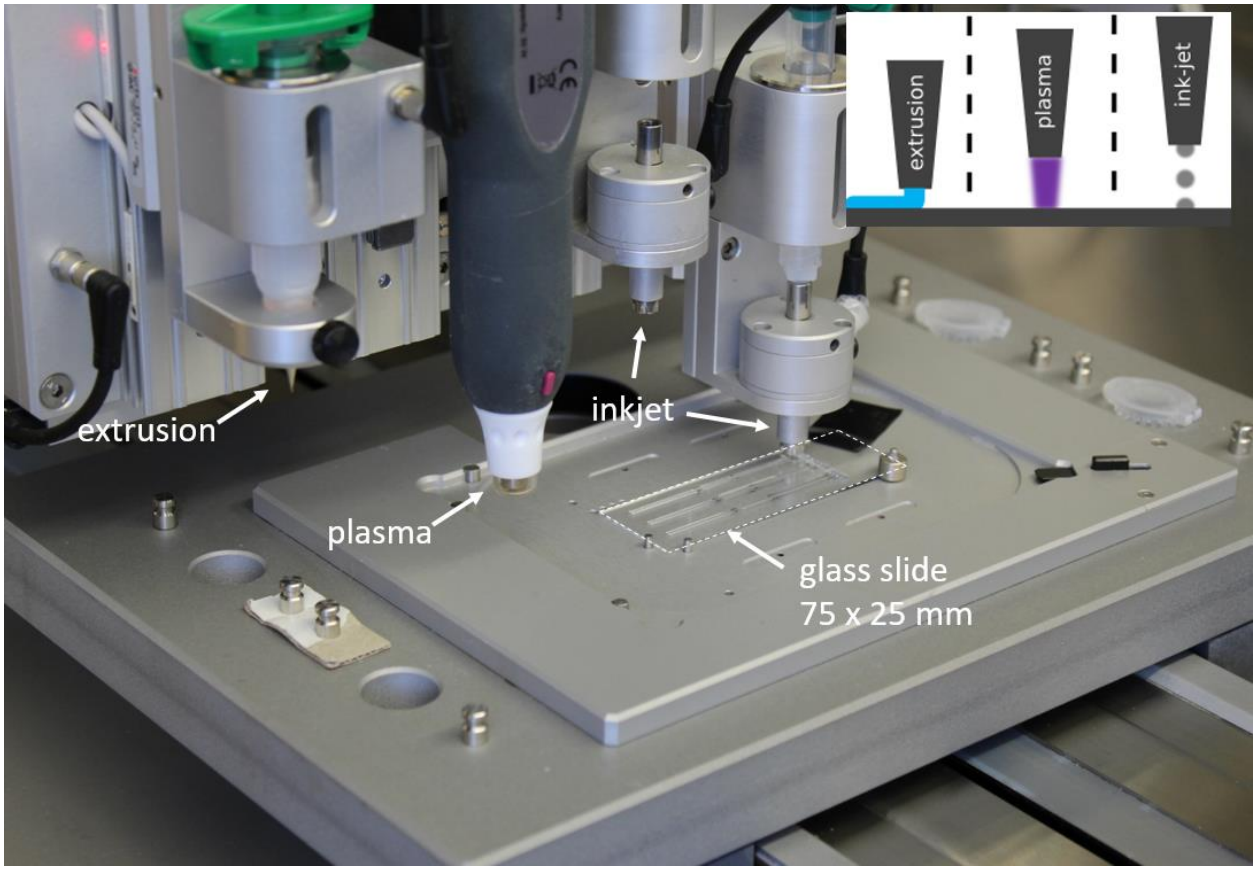

Supplementary Fig. 1: Hybrid printing platform.

The 3Ddiscovery is a modular 3D bioprinting platform from RegenHU, Switzerland. Our system supports four robot controlled print heads. Designs are printed on a substrate, in our case a microscope glass slide. Our instrument is configured to combine air pressure extrusion (direct dispenser print-head, RegenHU), two electromagentic ink-jet valves (cell-friendly print-head, RegenHU) and a plasma brush (Piezobrush®, Relyon). This allows us to handle paste and liquid inks and enables control over ink-ink wetting via plasma surface activation.

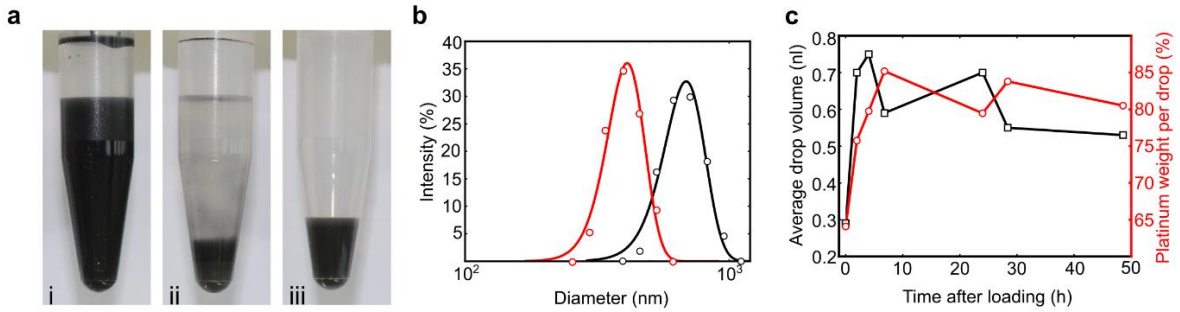

Supplementary Fig. 2: Platinum ink preparation and characterization.

a, photographs of a freshly sonicated platinum particle dispersion in TGME (i), sedimented dispersion (ii), and platinum particle slurry ready for loading in the printing head (iii). **b,** distribution of particle aggregate sizes before (black) and 1 h after tip sonication (red). **c,** Drop volume and platinum content (average from 5000 drops) as a function of the time after ink loading.

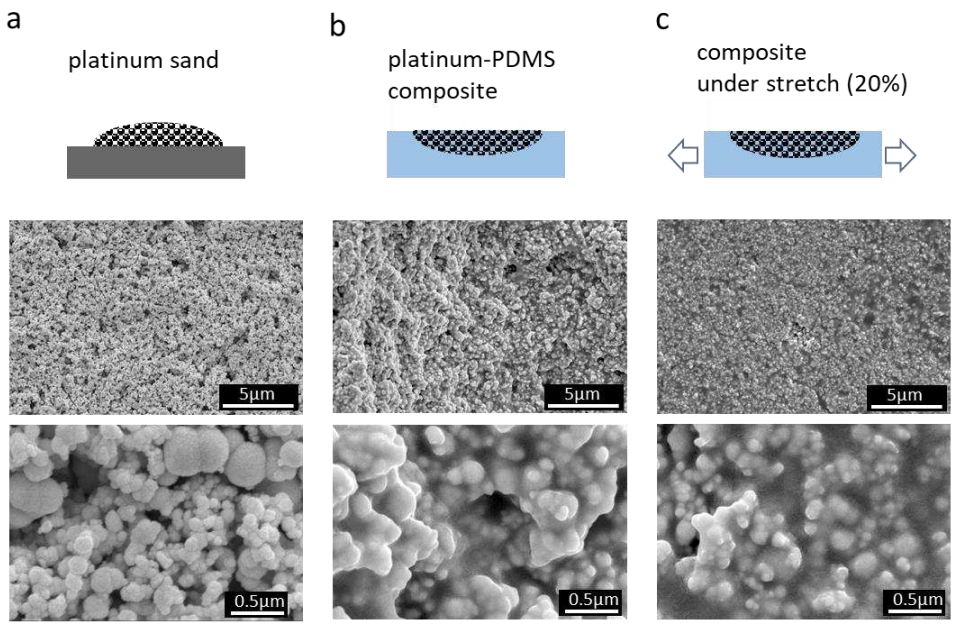

Supplementary Fig. 3: Electron microscopy of *in situ* formed Pt-PDMS composites.

a, platinum microparticle sand formed on glass following the evaporation of TGME solvent. High resolution images reveal that individual Pt particles form a percolating network. **b,** following infusion with PDMS and its polymerization, a composite material is created. High resolution images reveal that PDMS penetrates inter-particle spaces. **c,** the integrity of the composite material is maintained when global uniaxial strain of 20% is applied to the sample.

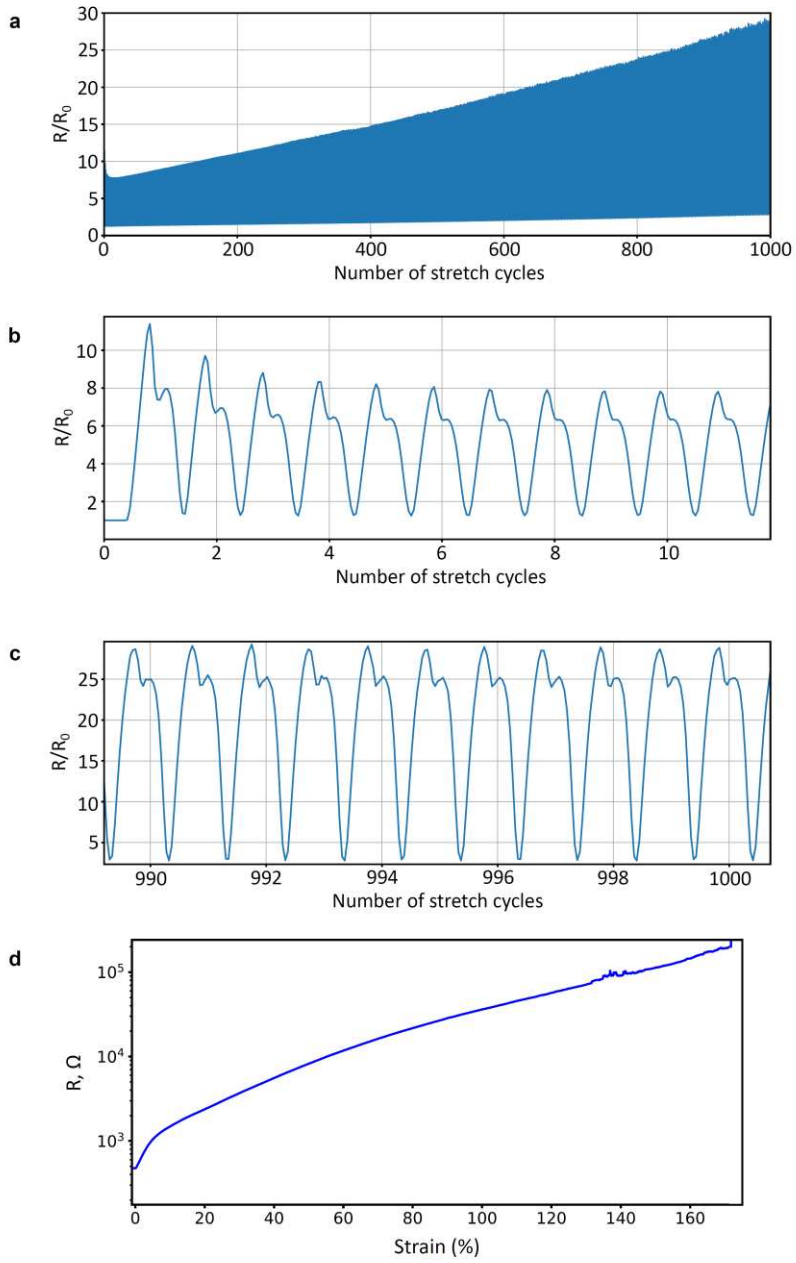

Supplementary Fig. 4: Electromechanical properties of *in situ* formed Pt-silicone composite conductors.

a, Change of electrical resistance of a line of Pt-silicone composite during cyclic stretching. Initial sample (gauge) length was 14 mm and the cross section area was 2.6 x 10^{-2} mm^2, (total length of the platinum composite conductor was 25 mm but 11 mm were embedded into the contacts and thus not stretched). One thousand strain cycles 0% - 20% - 0% were applied to the conductor at a rate of 0.5mm/s. **b,** behavior of the composite during the first 10 strain cycles. It is interesting to note that application of strain produces an "M" shaped response in the resistance of the composite conductor. This effect has been described in filled conductive rubbers [1]. A possible explanation is that initially, strain causes an increase of the separation between filler particles, which results in higher resistance. When strain is further increased, Poisson compression causes filler particles to come into contact again resulting in decreased resistance. The effect appears to be reversible upon strain release. **c,** behavior of the composite during the last 10 strain cycles. Strain induced changes of resistance for our material are significant but its durability compares well with recently

reported silver based extrudable inks [2]. **d**, a line of Pt-silicone composite is stretched to failure (same dimensions as in **a**). Mechanical and electrical failure occur simultaneously at strains beyond 100%. It is noted that such extreme elongation is unlikely to be encountered during normal *in vivo* use.

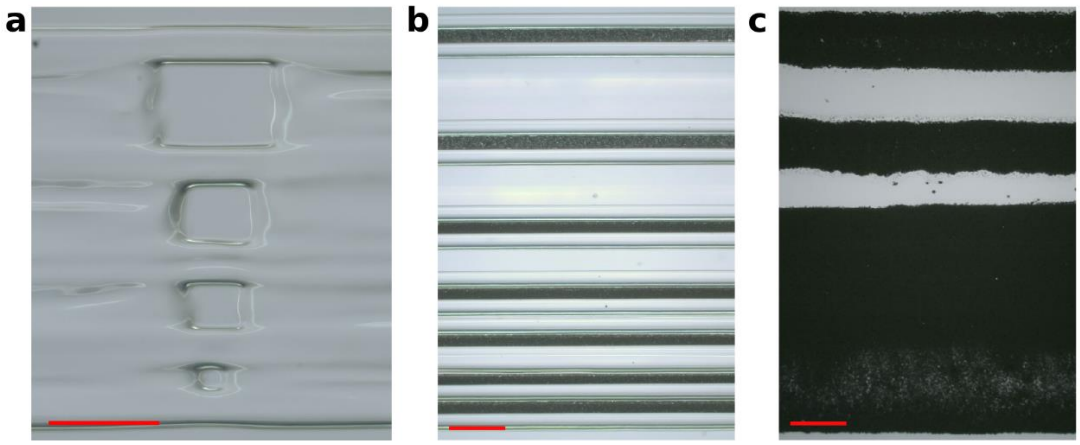

Supplementary Fig. 5: Integration density capability of NeuroPrint technology.

a, Using the SE1700 ink and an extrusion nozzle with inner diameter of 110 µm, we examined the resolution limits for creating openings (vias) in a continuous membrane. This defines the size of the smallest electrode active site achievable with the NeuroPrint technology. The width of the openings from top to bottom: 750µm, 510 µm, 400 µm, with the smallest opening 120 x 120 µm. Scale bar 750 µm. **b,** Using Ink-jet printing of platinum particle ink in between SE1700 borders we explore the resolution limits for patterning closely spaced interconnects. The distance between platinum lines from top to bottom is 1000, 800, 650, 450 and 400 µm, with the smallest achievable separation between conductive lines 280 µm. Scale bar 500 µm. **c,** When platinum dispersion ink is directly deposited on plasma treated silicone surface (without walls), closely spaced lines merge due to poor control over ink spreading. Scale bar 500 µm.

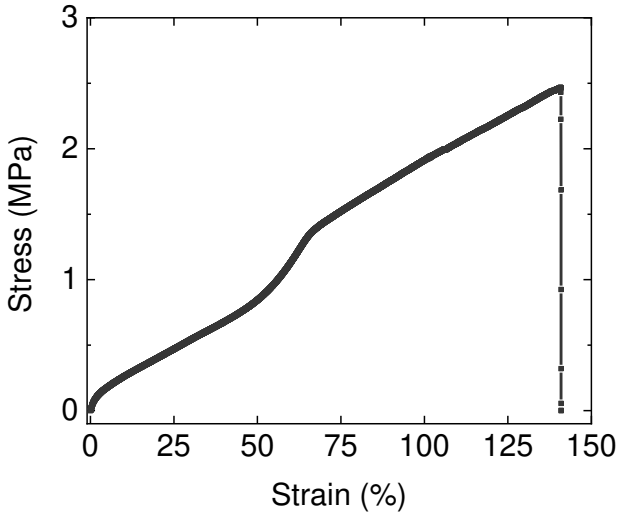

Supplementary Fig. 6: Stress-strain response of a typical array subjected to strain to failure.

Mechanical failure occurs well beyond 100%. Using the linear portion of the stress-strain curve (5-10% strain), we extract an elastic modulus of 1.98 MPa ± 0.35 (n = 10 tests of two separate arrays) for NeuroPrint arrays. Sample gauge length was 10 mm and the strain rate 0.1 mm/s.

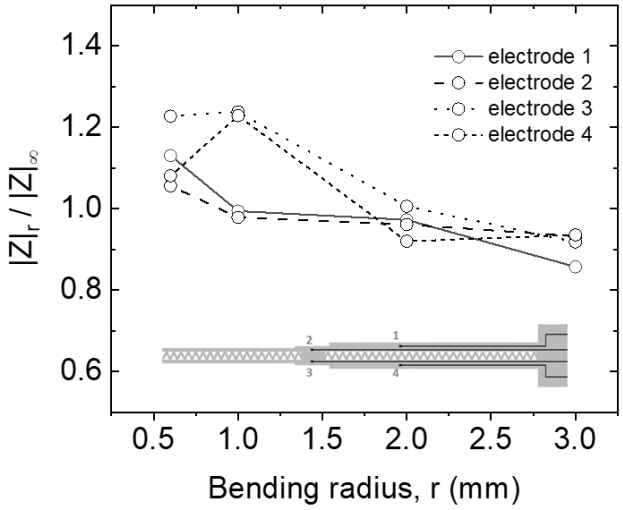

Supplementary Fig. 7: Bending test.

A typical NeuroPrint array (rat spinal cord design) is subjected to a bending test by wrapping the array around mandrels of different diameter. The impedance, $|Z|_\infty$ is obtained when the array is held flat. All values of |Z| are measured at 1kHz. The modest impedance change that results from bending indicates that arrays can be wrapped around small peripheral nerves with diameters of approximately 1 mm. Peripheral nerves vary significantly in diameter in the range of 20 - 0.2 mm [3].

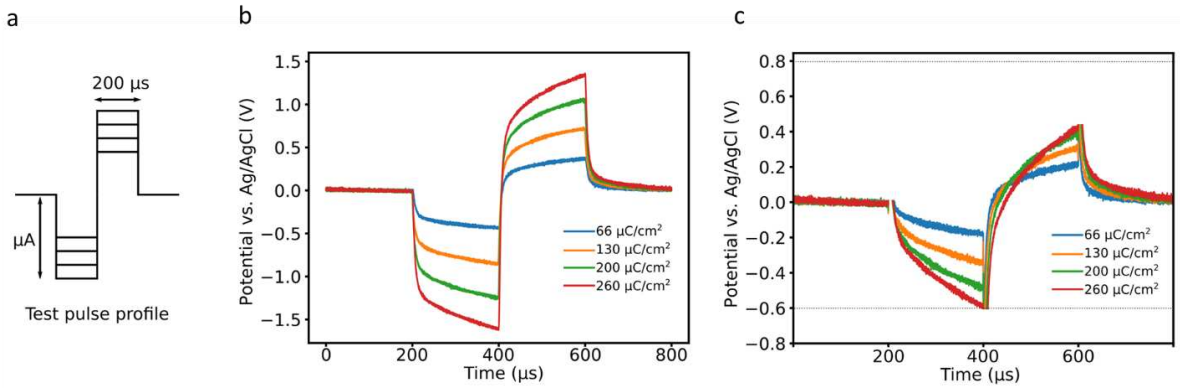

Supplementary Fig. 8: Determination of the charge injection limit.

a, the charge injection limit of electrodes is determined by supplying charge balanced biphasic current pulses of increasing amplitude. **b,** the resultant voltage traces are recorded vs. a Ag/AgCl reference electrode. This raw signal contains a contribution from the access voltage. The access voltage is due to resistive elements of the circuit and does not contribute to electrode surface polarization. The access voltage is thus subtracted according to the method proposed by Ganji *et al* [4]. **c,** the charge injection limit is reached when the electrode polarization crosses either the positive or negative threshold of the water window (+0.8V or -0.6V).

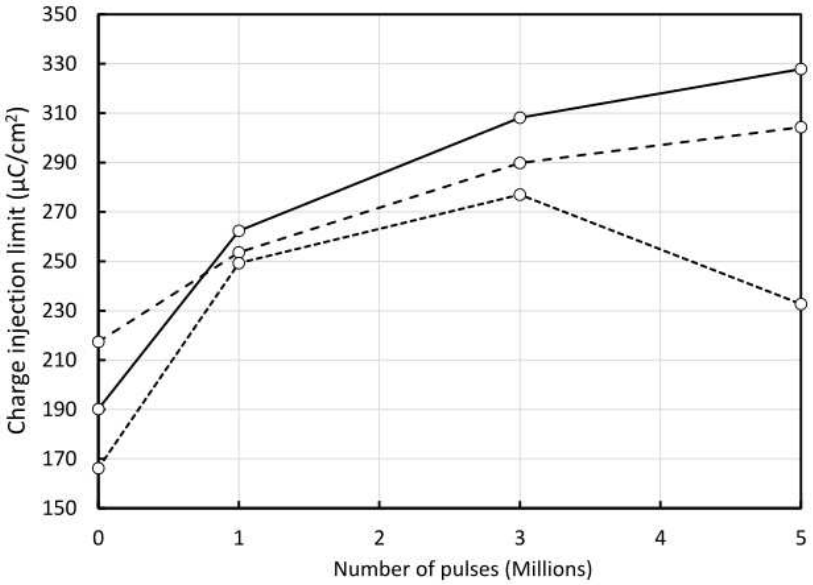

Supplementary Fig. 9: Stability of the Charge Injection Limit.

Charge injection limit of electrodes (n=3, individual electrodes from one array). The stability of individual electrodes under conditions of continuous stimulation was evaluated using trains of bi-phasic, charge balanced pulses (phase duration 200 µs, amplitude 100 µA, frequency 500 pulses/s) [5].

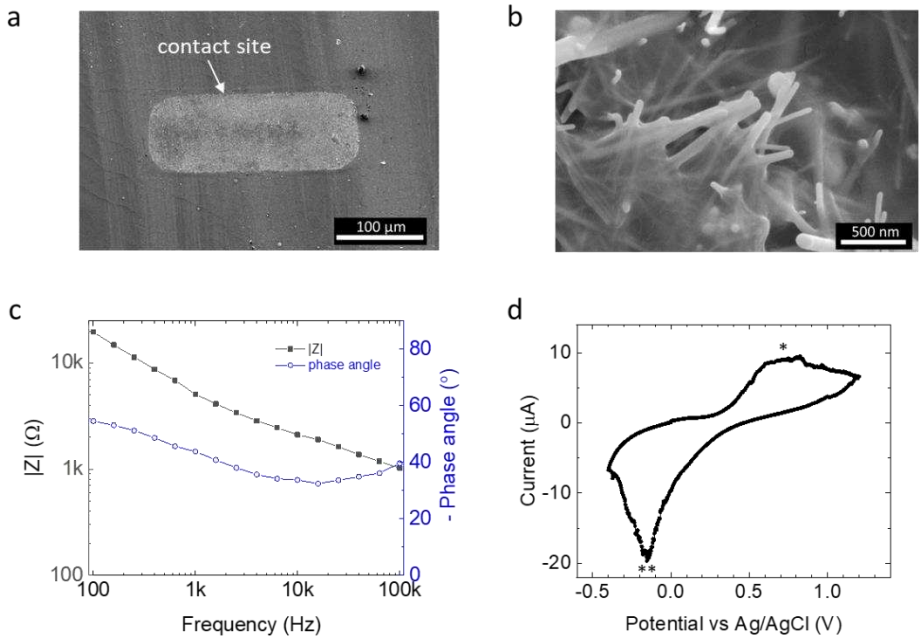

Supplementary Fig. 10: Alternative electrode materials.

a, SEM micrograph of an electrode contact site, where the conductive composite is formed from AgNW and silicone. The printing process is essentially the same as described for the platinum based composite. **b**, high magnification SEM micrograph illustrates the fine structure of the composite which is characterized by interlocked nanowires. The length of AgNW is in the range of 12 ± 2 µm. **c**, impedance spectra of electrodes utilizing AgNW are comparable to Platinum composites of similar size. **d**, cyclic voltammograms reveal oxidation (*) and reduction (**) electrochemical peaks typical for Ag. Cyclic voltammograms recorded in diluted sulfuric acid (300mM), at 1V/s.

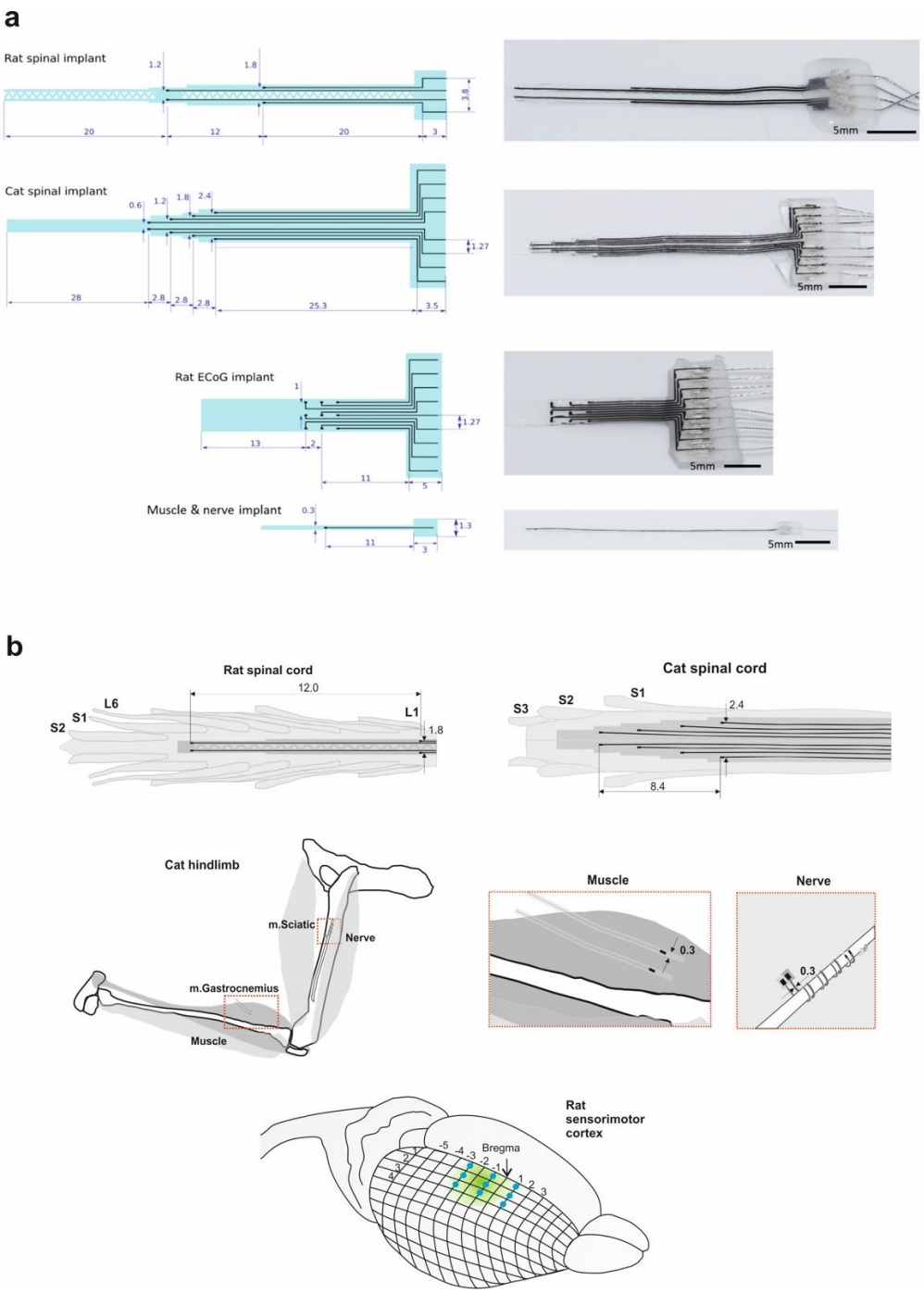

Supplementary Fig. 11: Catalogue of all types of implant produced .

a, Left panels show the overall layout and dimensions of all implant types. Silicone is shown in cyan, platinum – in black. The location of electrode opening sites are indicated as rectangles. All dimensions are in millimeters. Right panels are photographs of finished and connectorized devices ready for implantation. Muscle and nerve implants were produced in various lengths by modification of the CAD input files. The length was adapted to fit the various applications. For zebra fish experiments, the length was 44 mm, for other applications it was 11mm. **b**, The anatomic structure from the different animal models used to the application of customized NeuroPrint electrodes.

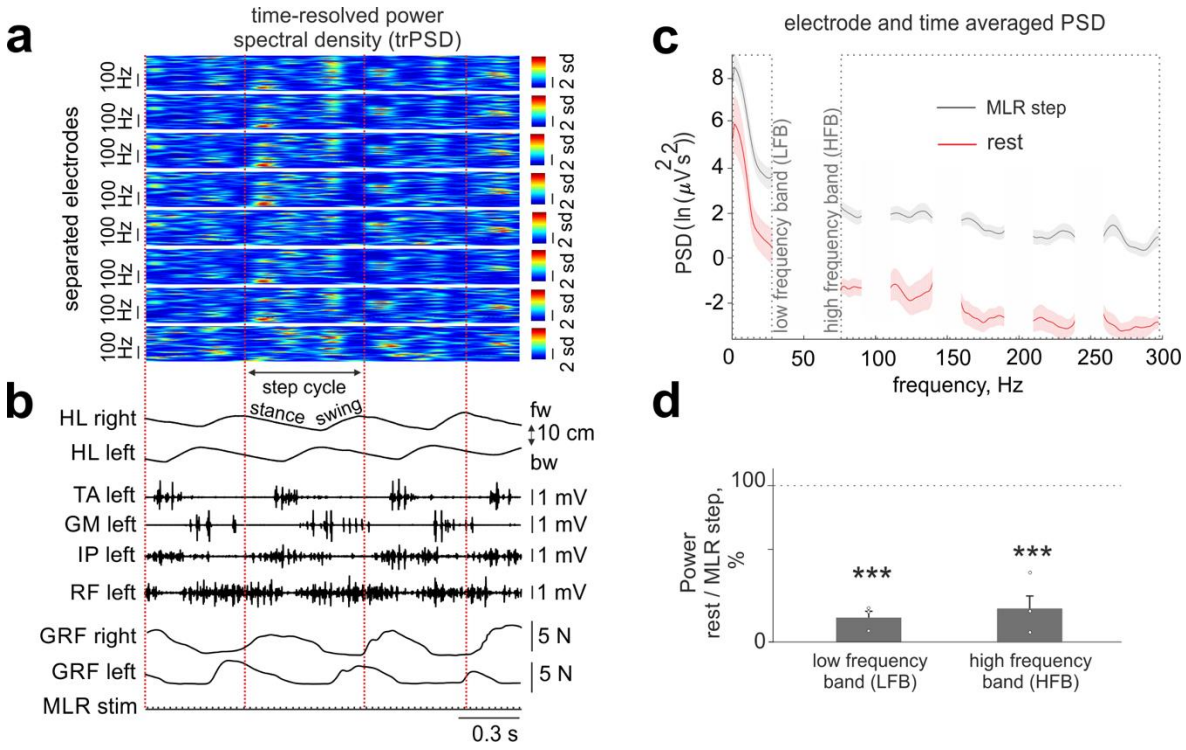

Supplementary Fig. 12: Monitoring of the spinal locomotor network facilitated by brain stem stimulation in cat.

a-b, Gait-modulated electrospinographic (ESG) activity recorded on 8 separated NeuroPrint array electrodes **(a)**, hind limbs (HL) anterior (A) and posterior (P) movements, EMG activity flexor (TA, m.tibialis anterior; IP, m.iliopsoas) and extensor (GM, m.gastrocnemius medialis; m.rectus femoris) muscles, and vertical ground reaction forces (GRF) **(b)** during stepping evoked by electrical stimulation of mesencephalic locomotor region (MLR). The ESG activity during MLR-evoked stepping was Fourier transformed into z-scored normalized time resolved power spectral densities (trPSD), shown in units of standard deviation (sd). **c,** PSD was calculated as trPSDs averaged across all timelines, electrodes and animals (n=3 cats). The data were divided to low frequency band (LFB, 2-25Hz) and high frequency band (HFB, 75-300Hz) to remove the effect of the 50Hz line noise. **d,** The PSD of ESG activity was substantially lower in both low frequency band (LFB) and high frequency band (HFB) during spontaneous activity in a resting animal in relation to MLR stimulation. Significance levels ***P <0.001.

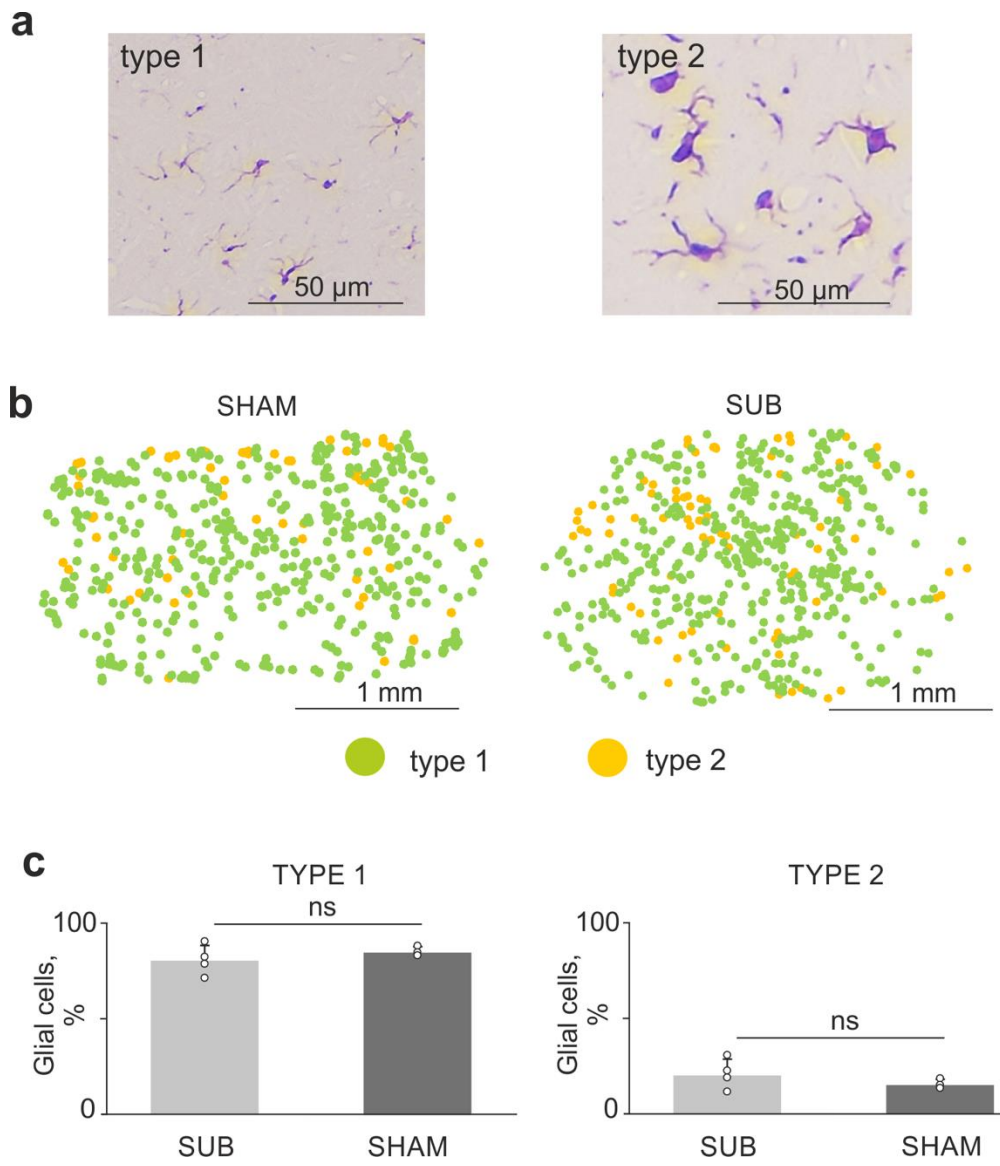

Supplementary Fig. 13: Immunohistochemical evaluation of the microglial cells subtypes in implanted and sham groups of animals 8 weeks after implantation.

a, A representative slices fragments of the spinal cord tissue located under the implants containing stained resting (Type 1) and activated (Type 2) microglial cells. **b,** Distribution of the resting and activating microglia in the spinal cord of subdurally implanted (SUB) and sham animals. **c**, Proportion of the resting and activated microglial cells populations in implanted and sham rats.

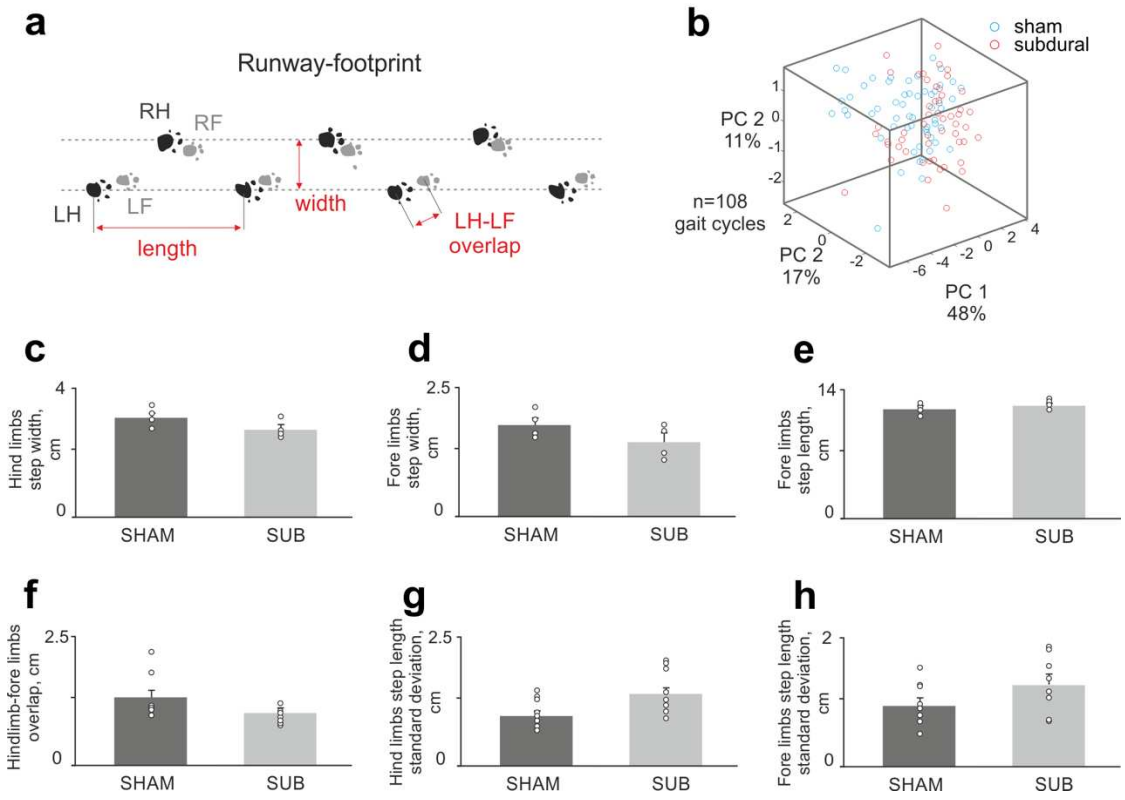

Supplementary Fig. 14: Evaluation of the sensorimotor control impairment during locomotion on the runway in implanted and sham groups of animals 8 weeks after implantation.

a, Foot positions (footprint) of the hind limbs and fore limbs during quadrupedal stepping on a runway. RH – right hindlimb, RF – right forelimb, LH – left hindlimb, LF – left forelimb. **b,** All the kinematic parameters computed for a minimum of 10 gait cycles per rat at 8 weeks post-implantation were subjected to a principal component (PC) analysis [6]. All gait cycles (n = 108, individual dots) from all tested rats (n = 4 per group) are represented in the new 3D space created by principal component analysis, PC1-3, which explained 76% of the total data variance. This analysis revealed that sham-operated rats and rats with NeuroPrint arrays exhibited similar gait patterns. (**c-f**), Varied characteristics of locomotor activity characterizing the separated forelimb and hindlimb locomotion and interlimb coordination. (**g-h**)**,** Standard deviations of the hind limbs and fore limbs step length, showing reproducibility of the stepping pattern.

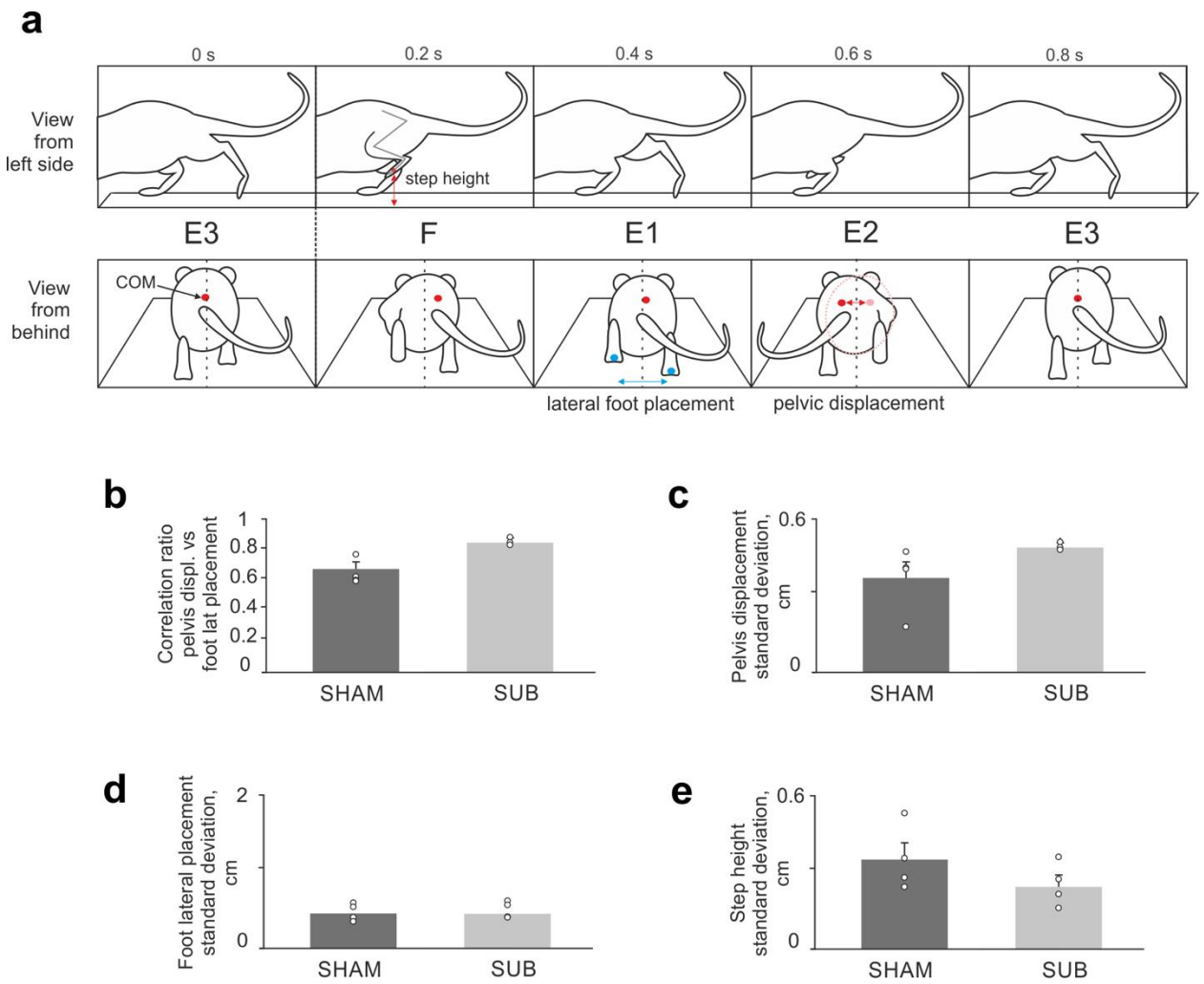

Supplementary Fig. 15: Evaluation of the postural imbalance during stepping on the treadmill belt in implanted and sham groups of animals 8 weeks after implantation.

a, Simultaneous analysis of the side view and back view of the rat stepping on the treadmill belt. E1-3, F – extension and flexion phases of the locomotor cycle. COM – center of mass. (**b-e**), Comparison of the varied aspects of integrative postural and locomotor control in implanted (n=3) and sham (n=4) groups of animals (n = 20-40 step cycles per rat). **b**, Correlation ratio between the pelvis displacement and foot lateral placement, corresponding to the efficacy of the dynamic balance control during stepping [7]. (**c-d**)**,** Standard deviations of pelvis displacement, foot lateral placement and step height showing variability and stability level of locomotor activity.

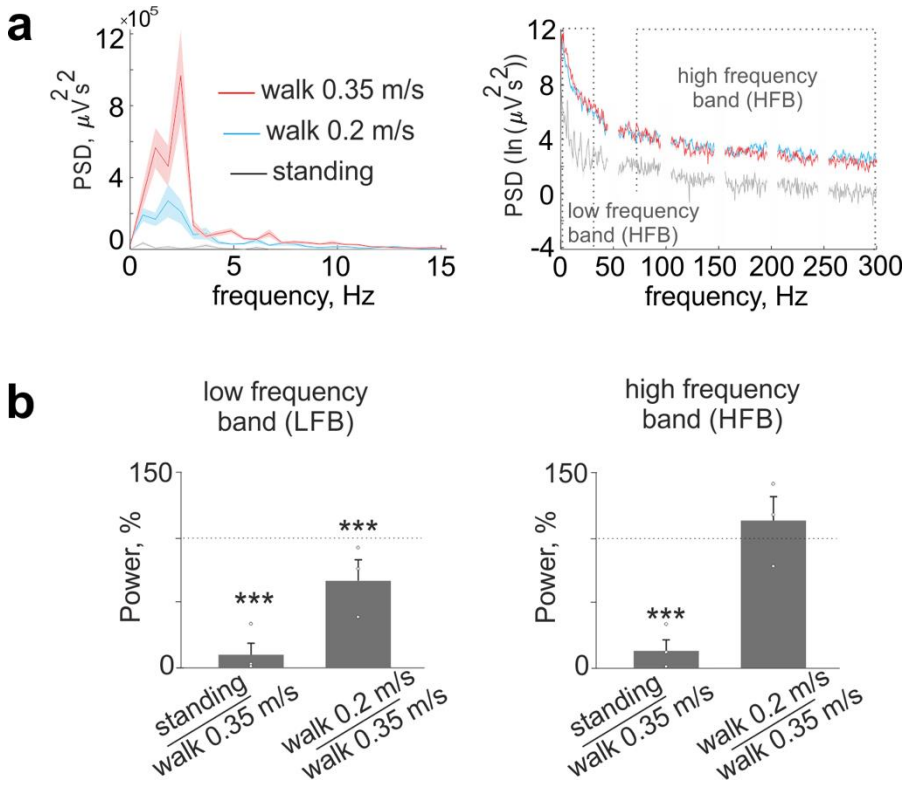

Supplementary Fig. 16: Rat task-specific spinal cord recording by NeuroPrint array.

a, Chronic (8 weeks) recordings of electrospinogram shown as power spectral density (PSD) averaged across all electrodes and animals (n=4) during standing and walking on the treadmill belt with two different speeds (0.2 m/s and 0.35 m/s). **b,** bar plots reporting means ± SE of power in low and high frequency bands during standing and slow walking (0.2 m/s) in relation to faster walking (0.35 m/s). Significance levels **P < 0.01; ***P <0.001.

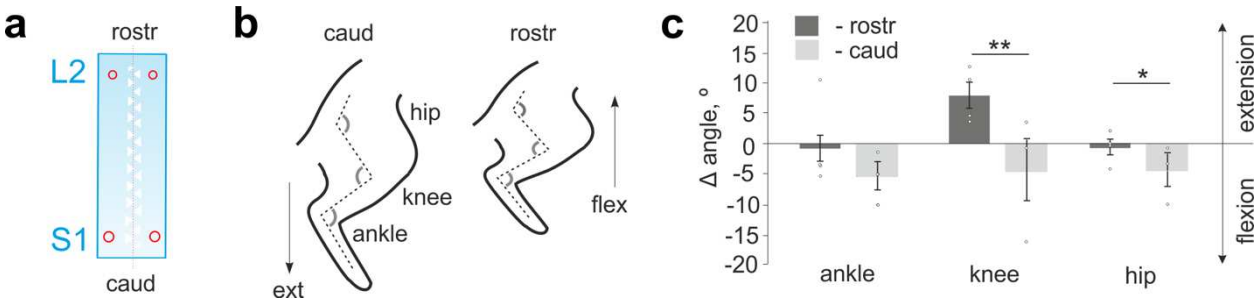

Supplementary Fig. 17: Site-specific spinal cord stimulation in chronic rat.

a-b, Site-specificity of the hindlimb motor evoked responses during rostral vs caudal stimulation. **c,** Averaged changes of ankle, knee and hip joints angles (n=4 rats) resulting from site-specific stimulation (1Hz, 0.3ms). Significance levels *P < 0.05; **P <0.01.

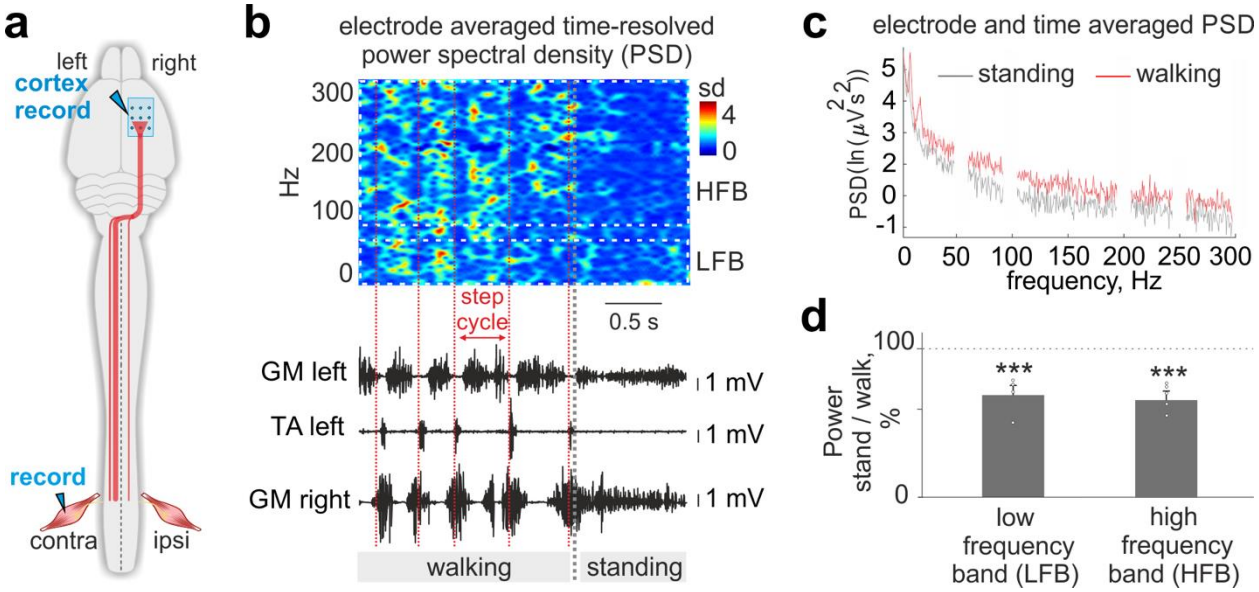

Supplementary Fig. 18: Chronic (6 weeks) electrocorticographic (ECoG) recording by NeuroPrint array in freely moving rat.

a, Position of the NeuroPrint array on the right motor cortex and its bilateral connection to the ipsi- and contralateral hindlimb muscles. **b,** Gait-modulated ECoG activity recorded by NeuroPrint array shown as electrode averaged z-score normalized time-resolved power spectral density (trPSD) and EMG activity of left (TA, m.tibialis anterior left; GM, m.gastrocnemius medialis left) and right (GM, m.gastrocnemius medialis right) muscles during walking on the runway and standing. **c,** trPSDs averaged across all electrodes and animals (n=4 rats). **d,** Bar plots reporting means ± SE of power in identified bands (n = 4 rats) show reduced power in low and high frequency bands during standing compared to walking. Significance levels ***P <0.001.

Supplementary Video 1. Hybrid printing technology for personalized soft neuromuscular interfaces (NeuroPrint).

Demonstration of multi-material printing. In order of presentation the video shows plasma surface activation, direct extrusion of silicones and jetting of platinum containing ink. The video is sped up to 3x.

Supplementary Video 2. Facilitation of spinal locomotor network by NeuroPrint array in motor impaired cat.

Supplementary Video 3. Long-term biointegration of the NeuroPrint technology: spontaneous stepping on a treadmill belt of the rat with implanted electrode shows no locomotor deficits.

Supplementary References:

1 Flandin, L., Hiltner, A. & Baer, E. Interrelationships between electrical and mechanical properties of a carbon black-filled ethylene–octene elastomer. *Polymer* **42**, 827-838, doi:https://doi.org/10.1016/S0032-3861(00)00324-4 (2001).

2 Matsuhisa, N. *et al.* Printable elastic conductors by in situ formation of silver nanoparticles from silver flakes. *Nature Materials* **16**, 834, doi:10.1038/nmat4904 https://www.nature.com/articles/nmat4904#supplementary-information (2017).

3 Lacour, S. P., Courtine, G. & Guck, J. Materials and technologies for soft implantable neuroprostheses. *Nature Reviews Materials* **1**, 16063, doi:10.1038/natrevmats.2016.63 (2016).

4 Ganji, M., Tanaka, A., Gilja, V., Halgren, E. & Dayeh, S. A. Scaling Effects on the Electrochemical Stimulation Performance of Au, Pt, and PEDOT:PSS Electrocorticography Arrays. **27**, 1703019, doi:10.1002/adfm.201703019 (2017).

5 Minev, I. R. *et al.* Electronic dura mater for long-term multimodal neural interfaces. *Science* **347**, 159-163, doi:10.1126/science.1260318 (2015).

6 Musienko, P. *et al.* Controlling Specific Locomotor Behaviors through Multidimensional Monoaminergic Modulation of Spinal Circuitries. *The Journal of Neuroscience* **31**, 9264-9278, doi:10.1523/jneurosci.5796-10.2011 (2011).

7 Musienko, P. *et al.* Somatosensory control of balance during locomotion in decerebrated cat. *Journal of Neurophysiology* **107**, 2072-2082, doi:10.1152/jn.00730.2011 (2012).